Copyright
by
Ganesh Borde
2024

The Report Committee for Ganesh Borde
certifies that this is the approved version of the following report:

Measurement of Markstein Numbers and Laminar Flame Speeds in Computationally Simulated Premixed Cylindrically Expanding Laminar Flames

APPROVED BY

SUPERVISING COMMITTEE:

Fabrizio Bisetti, Supervisor

Noel T. Clemens

Measurement of Markstein Numbers and Laminar Flame Speeds in Computationally Simulated Premixed Cylindrically Expanding Laminar Flames

by

Ganesh Borde

REPORT

Presented to the Faculty of the Graduate School of
The University of Texas at Austin
in Partial Fulfillment
of the Requirements
for the Degree of

MASTER OF SCIENCE IN ENGINEERING

THE UNIVERSITY OF TEXAS AT AUSTIN
December 2024

To Aai and Papa.

Acknowledgments

I would like to extend my sincere gratitude to my advisor, Dr. Fabrizio Bisetti for their invaluable guidance and support throughout my studies and research. His expertise in CFD, helped me a lot. I sincerely thank my colleague, Aditya Vinod, for his assistance with simulations and the many productive brainstorming sessions. I would also like to thank my report committee/reader Dr. Noel T. Clemens for the feedback that helped improve this report.

I am also grateful for the generous support of the Texas Advanced Computing Center (TACC) for providing the essential computing resources. Finally, I want to give very special thanks to my mother, my father, my brothers and sister, and my friends for their incredible support and encouragement.

Measurement of Markstein Numbers and Laminar Flame Speeds in Computationally Simulated Premixed Cylindrically Expanding Laminar Flames

Ganesh Borde, M.S.E.
The University of Texas at Austin, 2024

Supervisor: Fabrizio Bisetti

As global energy demands rise and concerns over fossil fuel emissions intensify, there is an urgent need to develop sustainable alternatives. Extensive research is being conducted to optimize hydrogen combustion. Key combustion properties, such as laminar flame speed and Markstein number, play crucial roles in characterizing premixed flames. These parameters influence flame stability, speed, and response to perturbations. While these properties can be determined experimentally, such measurements are often costly and subject to uncertainties. Numerical simulations, therefore, provide a valuable approach to studying these characteristics more efficiently.

In this work, a computational framework is developed to model cylindrically expanding laminar flames under constant pressure. This method avoids common instabilities encountered in ignition simulations. After validating the model against existing literature, the framework is applied to unity Lewis number mixtures of hydrogen and oxygen diluted with helium. These mixtures are studied at varying dilution levels, equivalence ratios, and pressures to understand their behavior in conditions relevant to the Von Kármán Combustion Chamber (VKCC), where the focus is on understanding the dynamics of turbulent flame fronts. The Markstein number is a critical parameter in assessing flame stability as it reflects the balance between diffusive and advective transport at the flame front. For all selected mixtures, the study found positive Markstein numbers, indicating stable behavior. Notably, as the equivalence ratio increases from 0.65 to 0.95, as the laminar flame speed and Markstein number increases.

Table of Contents

List of Tables

List of Figures

Chapter 1

Introduction

1.1 Background and motivation

As the world grapples with the urgency of reducing carbon emissions, the development and adoption of carbon-free fuels have become a critical focus in energy production. Hydrogen, with its potential to serve as a clean fuel, offers a promising pathway toward decarbonizing sectors traditionally reliant on fossil fuels. Hydrogen combustion produces only water as a byproduct, making it an ideal candidate for sustainable energy production without harmful carbon emissions. Current advancements in burner technology aim to optimize efficiency and reliability of hydrogen/ammonia combustion, demonstrating that hydrogen/ammonia can support the energy needs of society at scale.

Hydrogen's role in future energy systems is reinforced by the International Energy Agency's Global Hydrogen Review 2023 [12], which highlights hydrogen as central to achieving net-zero emissions and securing global energy supplies. Efforts to improve hydrogen-based combustion systems are instrumental in driving the energy industry towards adopting hydrogen as a viable fuel source and meeting the increasing demand for sustainable energy solutions.

The main motivation of this work rests in a distinct project aiming to investigate turbulent interface dynamics, which is significant for turbulent combustion as these interfaces impact the overall fuel burn rate. Various combustion regimes are influenced by how reactive fronts evolve, are formed and destroyed. Prior computational studies by Kulkarni et al. [17, 18, 16] analyzed the behavior of such interfaces in isotropic turbulence, establishing a basis for experimental research on turbulent interfaces within confined geometries, such as in a von Kármán Combustion Chamber (VKCC).

VKCC is a combustion device specifically designed to generate a stable turbulent shear flow generated by counter-rotating impellers. In the work by Vinod et al. [31], a turbulent von Kármán swirling flow is generated within a closed cylindrical chamber bounded by two counter-rotating disks. These disks, fitted with 16 curved blades, function as centrifugal pumps, drawing fluid in along the centerline and expelling it radially to create intense mixing. The disks have a radius of 0.925 times the cylinder's inner radius, and the spacing between them is 1.8 times this radius. This setup mirrors a widely-used experimental design for studying swirling flow dynamics. More geometry details are available in the supplementary material of [31].

In the VKCC, the goal is to create interfaces observable by imaging and laser diagnostics, such as particle image velocimetry (PIV) and planar laser-induced fluorescence (PLIF). In order to achieve this goal, low heat-release, premixed reactive mixtures were chosen to create stable interfaces without significant density variations, ensuring visibility, minimal thermodiffusive instability, and avoiding significant increase in pressure brought by combustion in a closed vessel. The Lewis number (Le), defined as the ratio of thermal diffusivity (α) to mass diffusivity (D), represents the relative rates of heat and mass diffusion. When Le $= 1$, both thermal and mass diffusivities are equal, leading to symmetric flame propagation. However, when Le $\neq 1$, mass and temperature diffuse at different rates, introducing additional physical processes that significantly impact flame propagation. One of them is the thermodiffusive instability (Markstein 1964; Sivashinksy 1977), which occurs due to imbalance between mass and thermal diffusion rates. In this work, the choice of unity Lewis number is justified by the objective to focus on solely on geometry-related stretch effects alone. The selected fuel/oxidizer mixtures selected described in section 1.11, are lean H_2/O_2 mixtures with unity Lewis number, achieved through high helium dilution.

The overarching goal of this work is to develop a framework for calculating the laminar flame speed and the Markstein number. Although the ultimate focus of this work is on turbulent combustion, the study of laminar flames is essential because they provide a fundamental reference for understanding flame dynamics in more complex turbulent environments.

Laminar flame speed serves as a key parameter in many turbulence models and is often used to define the flamelet regime of turbulent combustion. Similarly, the Markstein number characterizes the sensitivity of the flame to stretch and curvature, which are critical factors in turbulent flame propagation. Therefore, an accurate understanding of these laminar flame properties is necessary to establish a baseline for analyzing and predicting turbulent flame behavior. The following sections will explore the theory and relationships central to these parameters.

1.2 Laminar flame

A laminar flame is a type of flame in which the flow of the reacting gases is smooth and orderly, and the fluid flow is not in the turbulent regime. In the laminar regime, the premixed flame front propagates in a uniform and predictable manner, typically described by well-defined equations [22]. Key characteristics of a laminar flame include:

- **Flame front propagation:** The flame front generally propagates at a well-defined speed relative to the unburnt gas, known as the laminar flame speed. However, under certain conditions such as stretch, curvature, or instabilities, laminar flames may exhibit unsteady behavior.
- **Thin reaction zone:** The region where reactions occur is very thin, with sharp gradients in temperature and species concentrations between the burnt and unburnt gases.
- **Predictable structure:** In the absence of turbulence, the flame structure remains relatively smooth, and spatial distributions of velocity, temperature, and species concentrations are easier to predict and analyze compared to turbulent flames.

1.3 Definitions

The definitions of key metrics that describe premixed laminar flames are discussed here.

The laminar flame speed is defined as the speed of unburnt mixture normal to the flame surface relative to the local flow velocity [19]. It is denoted by S_L.

The flame thickness (δ_L) is a measure of the extent of a premixed flame. One of the most widely adopted definitions considers the gradient of the temperature distribution across the flame (along the normal to the flame sheet) $\partial T/\partial x$ as well as the unburnt (T_u) and burnt (T_b) gas temperatures [6]:

$$\delta_L = \frac{T_b - T_u}{\left(\frac{\partial T}{\partial x}\right)_{\max}}. \tag{1.1}$$

A schematic representation of Eq. 1.1 is shown in Fig. 1.1. The flame thickness as defined above is also known as the "thermal thickness" of the flame.

The flame time is a characteristic time defined as the ratio of flame thickness to laminar flame speed

$$\tau_L = \frac{\delta_L}{S_L}. \tag{1.2}$$

The flame time represents the time taken by a premixed flame to move a distance equal to the flame thickness.

The density ratio σ is the ratio of the densities of unburnt (ρ_u) to burnt (ρ_b) gases,

$$\sigma = \frac{\rho_u}{\rho_b}. \tag{1.3}$$

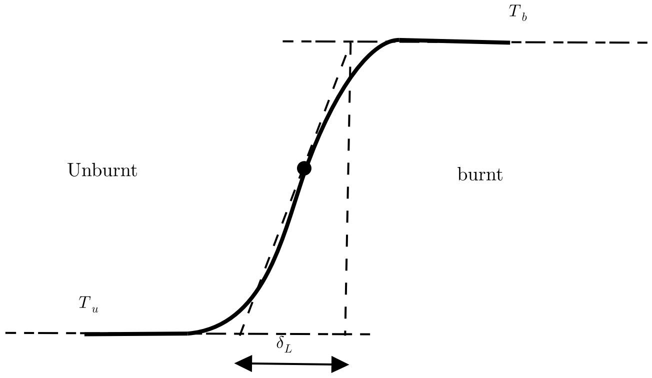

Figure 1.1: Spatial distribution of the temperature across a laminar premixed flame.

All laminar flames have a density ratio $\sigma > 1$.

1.4 Detailed structure

In this section we present an overview structure of an unstretched premixed laminar flame. An premixed hydrogen/air mixture with equivalence ratio $\phi = 0.5$ at standard temperature and pressure i.e. $T = 298$ K and $p = 1$ atm is chosen. The results presented are obtained using the Premixed package in Cantera [7]. A detailed mechanism by Burke et al. [2] is used in the analysis, and more details on this mechanism are discussed in Section 1.10. Fig. 1.2 illustrates the spatial distribution of temperature and gradient of temperature across the flame. Typically, the temperature starts from the unburnt gas, rises sharply in the flame front, and then reaches the adiabatic flame temperature in the burnt gas zone. The preheat zone shows relatively low temperatures as the unburnt mixture is heated by conduction from the flame

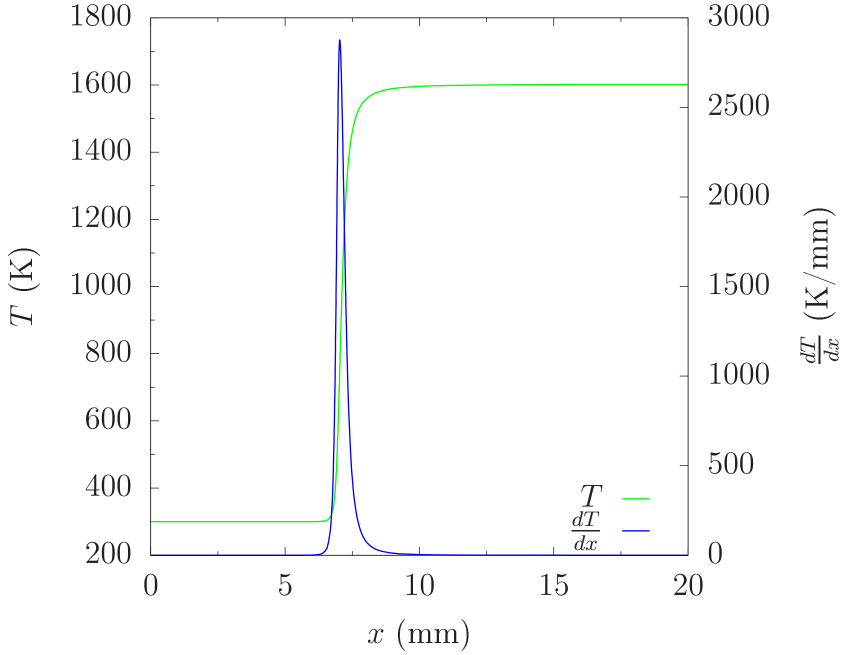

Figure 1.2: Temperature (T) and gradient of temperature (dT/dx) along the flame (x) for H_2/air premixed mixture with equivalence ratio $\phi = 0.5$ at 300 K and 1 atm.

front. The reaction zone exhibits a steep temperature rise, which marks the combustion process where heat is released due to chemical reactions. In the post-flame zone, the temperature remains relatively constant, representing hot burnt gases. The gradient of temperature along the flame profile (dT/dx) represents how rapidly the temperature changes spatially. The gradient is highest in the reaction zone, indicating rapid heat release and energy transfer in this region. Mole fractions of major species (H_2, O_2, N_2, and H_2O) and heat release rate (HRR) along the flame are shown in Fig. 1.3. Mole fractions of minor species, mainly radicals (OH, H, O, and HO_2) and HRR along the flame are

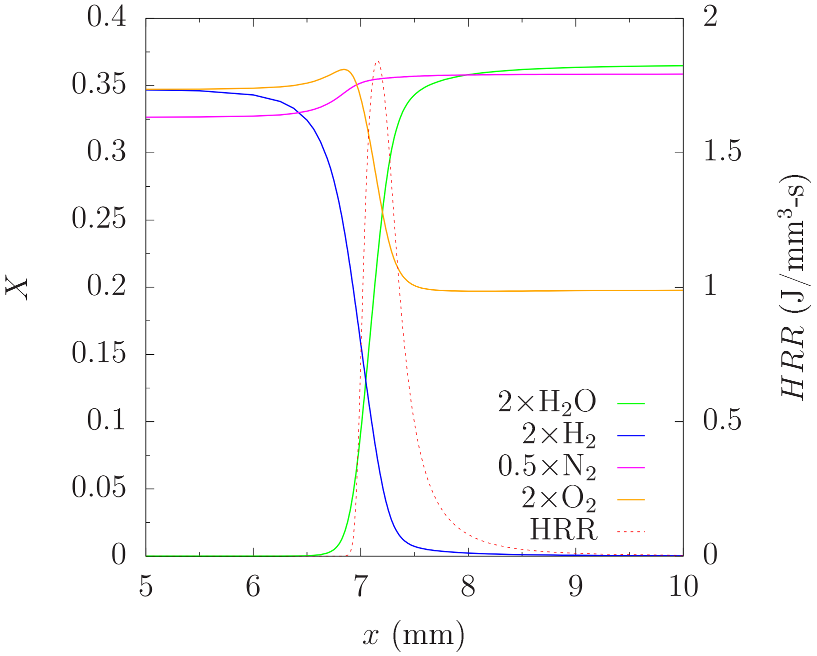

Figure 1.3: Mole fraction (X) of major species and HRR along the flame (x) for H_2/air mixture with equivalence ratio $\phi = 0.5$ at 300 K and 1 atm.

shown in Fig. 1.4, In the active reaction zone (i.e. at locations between 6 and 9 mm) the rapid rise in HO_2 mole fraction occurs slightly before the other species in the early stages of the reaction zone. However, HO_2 levels decline quickly after peaking, indicating that HO_2 plays a crucial but transient role during the early stages of the combustion process. Following the initial HO_2 formation, the production of H radicals dominates. The peak in H mole fraction coincides with the peak heat release rate, highlighting that H radical formation through chain branching is closely associated with the energy release in the flame. As the H radicals react with O_2, they lead to the generation of OH and O radicals through chain propagation reactions. The presence of OH and O marks the

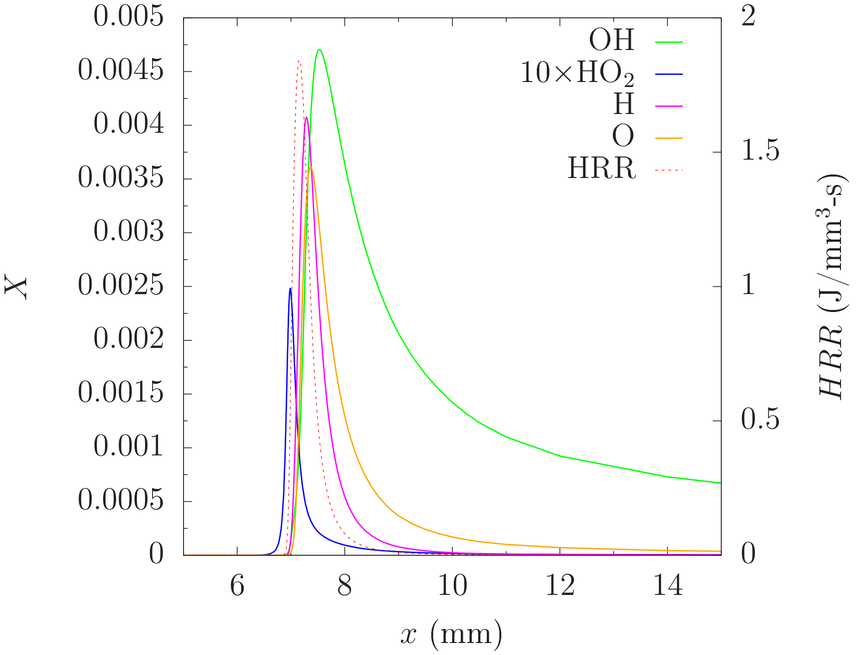

Figure 1.4: Mole fraction (X) of minor species and HRR along the flame (x) for H_2/air mixture with with equivalence ratio $\phi = 0.5$ at 300 K and 1 atm.

establishment of the flame's propagation mechanism, where the reaction rate and energy release are sustained. The HRR curve peaks sharply around the same location where H, OH, and O radicals are at their maximum concentrations, demonstrating that the heat released is directly related to these highly reactive species. Beyond 9 mm, the concentrations of these radicals diminish, and the HRR also declines, indicating that reactions are no longer contributing to the increase in temperature across the flame.

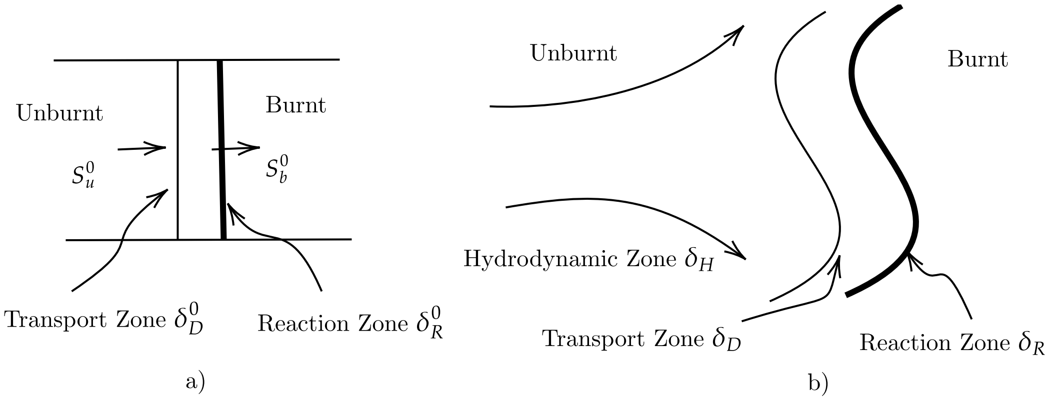

Figure 1.5: Schematic diagram of a) planar flame b) stretched laminar flame.

1.5 Stretched laminar flames

In Section 1.2, we presented the characteristics of a planar or unstretched laminar premixed flame, which represents the simplest mode of flame propagation. In such a configuration, the flame front is flat, and there are no external influences or geometrical variations on the flame surface affecting flame propagation. The flame moves at a constant speed (relative to the fluid) into the reactants, which is determined primarily by the thermodynamic properties of the reactants and products, as well as the chemical kinetics governing the combustion process. However, in practical combustion scenarios, flames are rarely flat. Instead, they are often subjected to stretch due to flow non-uniformities and flame curvature, leading to what is known as a stretched laminar flame. A comparison between stretched and unstretched laminar flames is shown in Fig. 1.5. Some basic definitions and mathematical models employed in the description of stretched laminar flames are discussed next.

1.5.1 Flame speed

Before defining the flame speed, a formal definition of the flame surface is required.

The flame surface corresponds to an iso-surface of the progress variable based on the temperature. In some studies the progress variable is based on the concentration of species. Let us consider a point on the flame surface, $T(x,t) = T^*$. At any location on this surface, the local gradient of temperature T defines the normal of the flame front as [26]

$$\mathbf{n} = -\frac{\nabla T}{|\nabla T|}, \tag{1.4}$$

where $\mathbf{n}$ points into the unburnt reactants as shown in Fig. 1.6. The flame speed (FS) is defined as the velocity component normal to the flame front, which can be written as [26]:

$$S_a = \mathbf{w} \cdot \mathbf{n}. \tag{1.5}$$

The flame speed is usually constant on the flame front if the flame is not thinned or thickened by the flow.

The flame displacement speed (FDS), S_d, as defined by Giannakopoulos et al. [6] as "The speed at which a iso-surface moves relative to the flow of reactants in the direction normal to the surface itself.", which can be written as [6]

$$S_d = S_a - \mathbf{v} \cdot \mathbf{n}, \tag{1.6}$$

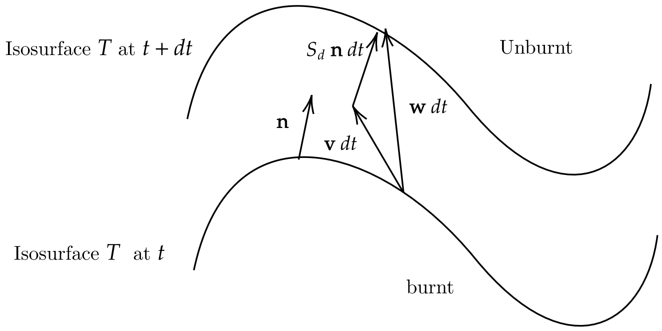

Figure 1.6: Schematic of quantities relevant to the definition of the flame speed [26].

where $\mathbf{v}$ is the local gas velocity.

1.5.2 Flame stretch

The flame stretch formulation is generalized by applying the transport theorem to a surface moving with an arbitrary velocity. A surface $A(t)$ is moving in space with an arbitrary velocity $\mathbf{w}$, and its normal vector is $\mathbf{n}$. Using the transport theorem, the stretch rate $\mathbb{K}$, as derived by Candel et al. [3]

$$\mathbb{K} = \frac{1}{\delta A}\frac{d(\delta A)}{dt} = -\mathbf{nn} : \nabla \mathbf{v} + \nabla \cdot \mathbf{v} + S_L \nabla \cdot \mathbf{n}. \tag{1.7}$$

The stretch formulation has concluded with three terms, the first term is normal element of the strain rate tensor, the second term is volumetric expansion of the fluid, and the last term is the curvature effects.

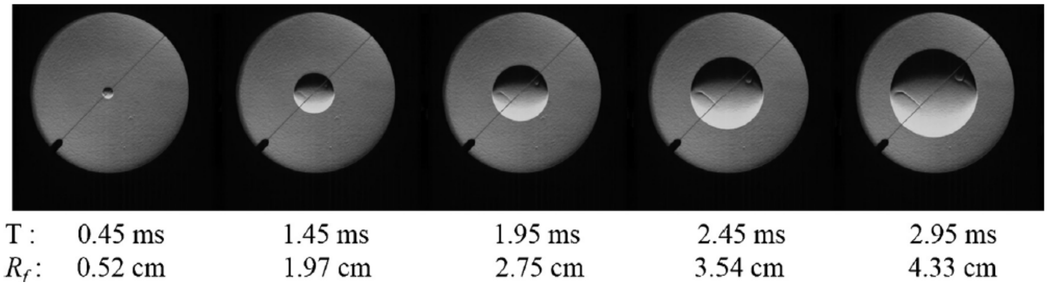

Figure 1.7: Schlieren image of a spherical expanding flame for H_2/air mixtures at equivalence ratio $\phi = 1$, $T = 298$ K, and $p = 1$ atm [11].

1.6 Spherical and cylindrical expanding flames

Expanding flames can take different geometrical forms based on the symmetry of the system:

- **Spherical Expanding Flames:** These flames propagate uniformly outward in all directions from a central ignition point, forming a spherical shape. Fig. 1.7 shows a schlieren image of a spherical propagating flame for H_2/air mixtures at $\phi = 1$, $T = 298$ K, and $p = 1$ atm, taken from Huo et al. [11].

- **Cylindrical Expanding Flames:** These flames propagate outward in a cylindrical shape, expanding radially while maintaining a consistent axis of symmetry. This geometry is often used in systems where one-dimensional or axisymmetric flame propagation is of interest.

The flame configuration of these expanding flames is shown in Fig. 1.8. Due to the simplicity of the geometry, the flame speed and stretch rate can be

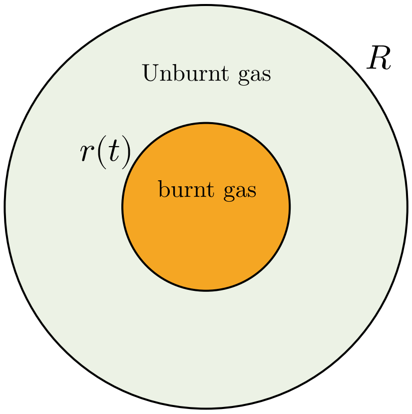

Figure 1.8: Flame configuration of expanding flames [6].

directly deduced from geometric considerations. The flame speed is defined as the rate at which the flame surface, $r(t)$, changes with respect to time, i.e.,

$$S_a = \frac{dr}{dt}. \tag{1.8}$$

Similarly, the flame displacement speed from Eq. 1.6 can be reduced to [6]

$$S_d = \frac{dr}{dt} - v_r, \tag{1.9}$$

where v_r is the velocity of the unburnt gases in the radial direction towards the flame.

The stretch rate depends on the geometry of the expanding flame. For a spherical expanding flame, it can be expressed as [26]

$$\mathbb{K} = \frac{1}{\delta A}\frac{d(\delta A)}{dt} = \frac{2}{r}\frac{dr}{dt}, \tag{1.10}$$

and for a cylindrical expanding flame, it is [26]

$$\mathbb{K} = \frac{1}{r}\frac{dr}{dt}. \tag{1.11}$$

1.7 Markstein theory

Markstein theory is a linear theory that relates the local flame speed S_f to the flame stretch $\mathbb{K}$ as

$$S_f = S_L - \mathcal{L}\mathbb{K}, \tag{1.12}$$

where $\mathcal{L}$ is the Markstein length. Physically, the Markstein length encapsulates the balance between diffusive and advective transport mechanisms at the flame front.

When $\mathcal{L} > 0$, the flame speed decreases with increasing stretch, indicating that diffusion stabilizes the flame against stretch effects. Conversely, if $\mathcal{L} < 0$, the flame speed increases with stretch, making the flame more susceptible to instabilities.

The above theory is modeled in different ways in the literature based on how the variables are defined, such as flame speed (FS) and flame displacement speed (FDS), which are detailed in the next two sections.

1.8 FDS relation

This relation is based on work by Giannakopoulos et al. [6]. In Markstein theory, when the local flame speed is defined by flame displacement speed, Eq. 1.12 becomes [6]

$$S_d^u = S_L^u - \mathcal{L}\mathbb{K}, \tag{1.13}$$

where the flame displacement speed on the unburnt side S_d^u is related as

$$S_d^u = \frac{\rho S_d}{\rho_u}, \tag{1.14}$$

where the displacement speed S_d is calculated based on Eq. 1.9.

Since the laminar flame speed calculated from the unstretched flame is on the unburnt side, we have $S_L^u = S_L$. Substituting the above relations into Eq. 1.13 and dividing by S_L, we obtain [6]

$$\frac{\widetilde{S}_d}{S_L} = 1 - \frac{\mathcal{L}}{\delta_L}\frac{\delta_L \mathbb{K}}{S_L}, \tag{1.15}$$

where $\widetilde{S}_d = S_d^u$.

The Markstein number is then calculated as [6]

$$\mathcal{M} = \frac{\mathcal{L}}{l_f} = \frac{\mathcal{L}}{\delta_L}\frac{\delta_L}{l_f}, \tag{1.16}$$

where l_f is the flame thickness defined by the diffusion length, i.e., $l_f = \frac{D_{th}^u}{S_L}$, and D_{th}^u is the thermal diffusivity of the unburnt gas.

1.9 FS relation

The following formulation was developed based on the work of Huo et al. [11]. In Markstein theory, when the local flame speed is defined by flame speed, Eq. 1.12 becomes [11]

$$S_a^b = S_L^b - \mathcal{L}^b\mathbb{K}, \tag{1.17}$$

where S_a^b is the flame speed calculated on the burnt side

$$S_a^b = \frac{dr}{dt}, \tag{1.18}$$

and S_L^b is laminar flame speed calculated on the burnt side of the flame, which can be related to S_L as

$$S_L^b = \sigma S_L. \tag{1.19}$$

Dividing Eq. 1.17 by S_L^b gives

$$\frac{S_a^b}{S_L^b} = 1 - \frac{\mathcal{L}^b}{\delta_L}\frac{\delta_L \mathbb{K}}{S_L^b}. \tag{1.20}$$

Finally, the Markstein number is calculated as

$$\mathcal{M}^b = \frac{\mathcal{L}^b}{\delta_L}. \tag{1.21}$$

The relation in Eq. 1.20 varies depending on how the stretch rate is defined, which is discussed below. In the linear stretch (LS) extrapolation model, the stretch rate is defined in Eqs. 1.11 and 1.10.

1.10 Chemistry mechanisms

Multiple mechanisms exist to describe the chemical reactions occurring in gas mixtures, each varying in complexity and scope. These models range from simple global reaction mechanisms to detailed mechanisms that consider numerous individual species and reactions. For example, reduced mechanisms simplify the reaction network while maintaining essential dynamics, whereas comprehensive mechanisms, such as GRI-Mech for combustion, provide a detailed representation of species interactions and reaction rates. The choice of mechanism depends on the specific application and the desired balance between computational cost and accuracy. In this work, we use four different mechanisms:

- Li et al. [23] — An updated comprehensive kinetic model of hydrogen combustion. This mechanism has 11 species and 19 reactions.
- Hong et al. [10] — An updated H_2/O_2 reaction mechanism that incorporates recent reaction rate determinations in shock tubes from laboratory experiments. This mechanism consists of 10 species and 20 reactions.
- Burke et al. [2] — An updated H_2/O_2 kinetic model based on that of Li et al. The primary motivations for the model revision are to incorporate recent improvements in rate constant treatments and resolve discrepancies between experimental data and predictions using recently published kinetic models in dilute, high-pressure flames. This mechanism consists of 13 species and 19 reactions.
- UCSD [30] — Chemical-Kinetic Mechanisms for Combustion Applications developed at the University of California, San Diego. This mechanism consists of 58 species and 270 reactions.

1.11 Mixture Selection

The work presented in this section is based on the work of Aditya Vinod, a doctoral candidate at The University of Texas at Austin. The description of the mixture selection is included here to ensure continuity and provide clarity for the reader.

The objective is to select unity Lewis number mixtures to minimize thermodiffusive instabilities in the VKCC. This was achieved by adding helium as a diluent to the hydrogen/oxygen mixture. Different combinations of equivalence ratio ϕ and helium mole fraction in the oxidizer ϑ were studied using Cantera [7]. Figure 1.9 illustrates the Lewis number in the ϕ-ϑ space, where points marked in magenta indicate unity Lewis number mixtures.

It was observed that varying pressure does not affect the Lewis number. From these mixtures, a subset with constant dimensionless parameters for $T_u = 300$ K was selected, as shown in Table 1.1. They are named as DXXEYY, where XX is $\vartheta \times 100$ and YY is $\phi \times 100$.

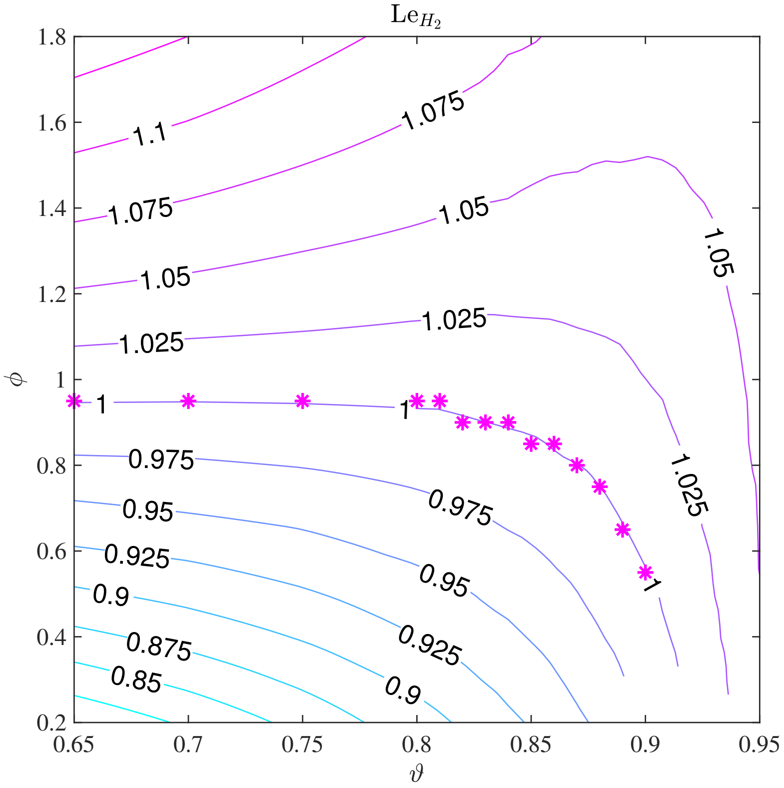

Figure 1.9: Lewis number $\mathrm{Le}_{\mathrm{H}_2}$ lines in ϕ-ϑ for mixtures at $p = 1$ atm and $T_u = 300$ K.

Table 1.1: Table of selected mixtures with Le ≈ 1 and constant dimensionless parameters for $T_u = 300$ K.

Name	ϑ	ϕ	X_{He}	$X_{\mathrm{O_2}}$	$X_{\mathrm{H_2}}$	$\mathrm{Le}_{\mathrm{H_2}}$	$\mathrm{Le}_{\mathrm{O_2}}$	Pr	$\mathrm{Sc}_{\mathrm{O_2}}$	p_0 (atm)	σ	S_L (m/s)	δ_L (mm)	τ_L (ms)	$\alpha\tau_L$
D80E95	0.80	0.95	0.5797	0.1449	0.2754	1.002	1.586	0.526	0.834	1.000	7.604	3.708	0.567	0.153	1.130
D82E90	0.82	0.90	0.6193	0.1360	0.2447	0.998	1.627	0.531	0.864	1.000	7.380	3.216	0.617	0.192	1.104
D84E90	0.84	0.90	0.6522	0.1242	0.2236	1.002	1.678	0.539	0.904	1.000	7.167	2.832	0.673	0.238	1.076
										2.000	7.227	2.990	0.282	0.094	0.987
D89E65	0.89	0.65	0.7787	0.0962	0.1251	0.999	1.831	0.558	1.022	1.000	5.140	1.097	0.951	0.867	0.963
										2.000	5.140	0.304	0.435	0.420	0.928
										3.000	5.141	0.201	0.284	0.293	0.912

1.12 Objective and Outline

The overall objective is to develop a framework for calculating laminar flame speeds and Markstein numbers and to apply this framework to premixed hydrogen/oxygen mixtures diluted with helium (selected mixtures) in cylindrically expanding flames. This objective will be achieved by completing the following tasks:

- Conducting an extensive study to determine the appropriate relation for calculating Markstein numbers.
- Initializing the flame and implementing the Soret effect in the numerical solver.
- Validating the numerical solver through a convergence study and comparing the results with existing literature.
- Applying the developed framework to calculate the properties of the selected mixtures.

The structure of the report is as follows. Chapter 2 provides an explanation of the governing equations and the numerical solver. Chapter 3 focuses on the validation of the solver. Finally, Chapter 4 presents the results, conclusions, and potential future work for this research.

Chapter 2

Governing equations and numerical solver

This chapter provides a comprehensive overview of the governing equations used to model the complex physics of reactive flows. It discusses the methods for implementing these equations into a numerical solver, detailing how they are discretized and solved to capture the dynamics of reactive processes. Furthermore, the chapter introduces techniques for post-processing the raw data generated by simulations.

2.1 Governing equation

The fully conservative finite difference scheme for incompressible flow simulations by Morinishi et al. [25] is used in the solver. Using the higher order accurate finite difference schemes for the non-linear convective term in the Navier-Stokes equations suffers from an aliasing error. To overcome this error, second order finite difference schemes on a staggered grid arrangement are employed [5].

The variable density, low Mach number Navier-Stokes equations are expressed as follows. The conservation of mass is given by [5]

$$\frac{\partial \rho}{\partial t} + \nabla \cdot (\rho \mathbf{u}) = 0, \tag{2.1}$$

where $\mathbf{u}$ is the velocity vector and ρ is the mixture density. Similarly, the conservation of momentum is given by [5]

$$\frac{\partial(\rho\mathbf{u})}{\partial t} + \nabla\cdot(\rho\mathbf{u}\otimes\mathbf{u}) = -\nabla p + \nabla\cdot\boldsymbol{\sigma}, \tag{2.2}$$

where p is the pressure, and $\boldsymbol{\sigma}$ is the stress tensor given by [5]

$$\boldsymbol{\sigma} = \mu\left(\nabla\mathbf{u} + (\nabla\mathbf{u})^T\right) - \frac{2}{3}\mu(\nabla\cdot\mathbf{u})\mathbf{I}. \tag{2.3}$$

In momentum equation Eq. 2.3, μ is the mixture dynamic viscosity and I is the identity tensor. The conservation of energy with constant pressure approximation is [5]

$$\frac{\partial\rho h}{\partial t} + \nabla\cdot(\rho h\mathbf{u}) = -\nabla\cdot\mathbf{q}, \tag{2.4}$$

where h is the enthalpy, and $\nabla\cdot\mathbf{q}$ is source term. The transport equation is [5]

$$\frac{\partial\rho Z}{\partial t} + \nabla\cdot(\rho\boldsymbol{u}Z) = \nabla\cdot(\rho D_Z\nabla Z) + \dot{\omega}, \tag{2.5}$$

where D_Z is the diffusivity. Here $\rho = \widehat{\rho}(Z)$, $\mu = \widehat{\mu}(Z)$,$D_Z = \widehat{D}_Z(Z)$, and $\dot{\omega}$ are density, viscosity, diffusivity and chemical source term respectively. The modeling of species diffusion velocities is is approximated using different models; generally, two models are used: multicomponent transport and mixture-averaged transport. In this work, the mixture-averaged transport model is used, which will be presented in detail in the next section.

2.2 Mixture-average transport

This section describes approximate (mixture-averaged) methods to determine transport properties in a mixture from the pure species values and binary diffusion coefficients. These technique offers accurate, and less computational cost compared to multicomponent transport [28]. The transport equations are explained below.

Models for $\mathbf{V}_i$, the species diffusion velocity, are based on the uncorrected species diffusion velocity $\mathbf{V}_i^0$, here only mass diffusion is considered. The model defined in the work by Kuo [13]:

$$\mathbf{V}_i^0 = -D_i \frac{\nabla X_i}{X_i} = -D_i \frac{\nabla Y_i}{Y_i} - D_i \frac{\nabla W}{W}, \tag{2.6}$$

where W is the molecular mass of the mixture and D_i is the species mixture-averaged diffusion coefficient. The Hirschfelder and Curtiss approximation is adopted for D_i [8]. The species diffusion velocity is approximated as $\mathbf{V}_i = \mathbf{V}_i^0 + \mathbf{u}^c$, where $\mathbf{u}^c$ is the correction velocity defined as:

$$\mathbf{u}^c = -\sum_i Y_i \mathbf{V}_i^0. \tag{2.7}$$

Then the transport equation Eq. 2.5 for Y_i becomes:

$$\begin{aligned} \frac{\partial \rho Y_i}{\partial t} + \nabla \cdot (\rho \mathbf{u} Y_i) &= -\nabla \cdot (\rho Y_i \mathbf{V}_i) + \dot{\omega}_i && (2.8) \\ &= \nabla \cdot (\rho D_i \nabla Y_i) \nabla \cdot (\rho Y_i \mathbf{u}^c) + \nabla \cdot \mathbf{j}_i^m + \dot{\omega}_i, && (2.9) \end{aligned}$$

where

$$\mathbf{j}_i^m = \rho D_i Y_i \frac{\nabla W}{W}. \tag{2.10}$$

The transport equation for enthalpy (at constant pressure) results

$$\begin{aligned} \frac{\partial \rho h}{\partial t} + \nabla \cdot (\rho h \mathbf{u}) &= \nabla \cdot (\rho D_{th} \nabla h) - \nabla \cdot (\rho h \mathbf{u}^c) \\ &\quad + \nabla \cdot \left(\sum_i h_i \mathbf{j}_i^m \right) - \nabla \cdot \left(\sum_i h_i \rho (D_{th} - D_i) \nabla Y_i \right) + \dot{\omega}_i^h. \end{aligned} \tag{2.11}$$

2.3 Soret effect

The Thermal diffusion also known as Soret effect is the occurrence of a diffusion flux due to a temperature gradient. This effects plays a role where there is heavy or light fuel in the mixtures. Traditional mixture-averaged diffusion models assumption neglect thermal diffusion. A brief review by Liang et al. [24], have addressed that Soret effect plays an important role in determining the flame speeds, laminar flame speeds and Markstein numbers.

As explained in the above section i.e. combustion model using mixture-average transport, which does not included the thermal diffusion. In this section we include the Soret effect to model the mixture-average transport. In the Eq. 2.6 add the thermal diffusion, which gives the uncorrected velocity $\mathbf{V}_i^0$ as presented by Kuo [13]:

$$\mathbf{V}_i^0 = -D_i^m \frac{\nabla X_i}{X_i} - \frac{D_i^T}{\rho Y_i}\frac{\nabla T}{T} = -D_i^m \frac{\nabla Y_i}{Y_i} - D_i^m \frac{\nabla W}{W} - \frac{D_i^T}{\rho Y_i}\frac{\nabla T}{T}, \tag{2.12}$$

where D_i^T is species thermal diffusion coefficient will be discussed later. The correction velocity contains two different correction given as

$$\mathbf{u}_c = \mathbf{u}_c^m + \mathbf{u}_c^T, \tag{2.13}$$

where $\mathbf{u}_c^m$ is correction due to mass diffusion and $\mathbf{u}_c^T$ is correction due to thermal diffusion, as given the correction are evaluated by equation Eq. 2.7, yielding

$$\mathbf{u}_c^m = \sum_i D_i \nabla Y_i + \frac{\nabla W}{W} \sum_i D_i Y_i, \tag{2.14}$$

and

$$\mathbf{u}_c^T = \frac{1}{\rho}\frac{\nabla T}{T}\sum_i D_i^T. \tag{2.15}$$

The transport equation for Y_i Eq. 2.5 can be reduced to:

$$\begin{aligned}\frac{\partial \rho Y_i}{\partial t} + \nabla\cdot(\rho\mathbf{u}Y_i) = -\nabla\cdot(\rho D_i \nabla Y_i) - \nabla\cdot(\rho Y_i \mathbf{u}^c)\\ + \nabla\cdot(D_i^T\frac{\nabla T}{T}) + \nabla\cdot\mathbf{j}_i + \dot{\omega}_i,\end{aligned} \tag{2.16}$$

In enthalpy transport Eq. 2.17 substituting the Eq. 2.12 results

$$\begin{aligned}\frac{\partial \rho h}{\partial t} + \nabla\cdot(\rho h\mathbf{u}) = \nabla\cdot(\rho D_{th}\nabla h) - \nabla\cdot(\rho h\mathbf{u}^c)\\ + \nabla\cdot\left(\sum_i h_i \mathbf{j}_i^m\right) + \nabla\cdot(\sum_i h_i D_i^T \frac{\nabla T}{T})\\ - \nabla\cdot\left(\sum_i h_i \rho(D_{th} - D_i)\nabla Y_i\right) + \dot{\omega}_i^h,\end{aligned} \tag{2.17}$$

where D_i^T is the thermal diffusion coefficient of species i, units of $\mathrm{kg\,m^{-2}\,s^{-1}}$. It is determined using multicomponent and mixture-averaged approximations, they are briefly expalined in the work by Schlup et al. [28].

2.4 Thermal diffusion coefficient

The species thermal diffusion coefficient is calculated from multicomponent transport properties based on studies conducted several decades ago [9, 15]. In these studies, the thermal diffusion coefficients are computed by solving a system of equations. The subroutine used to calculate the thermal diffusion coefficient D_i^T is available in Chemkin, a software tool for solving complex chemical kinetics and reacting flow problems [14], and is named “MCMCDT”.

Given the pressure, temperature, and species mole fractions, this subroutine returns the species thermal diffusion coefficient. Results obtained using this approach are referred to as MA-MC.

The mixture-averaged thermal diffusion model introduced by Chapman and Cowling [4] was selected as it eliminates the need for pre-simulation of thermal diffusion coefficients via multicomponent transport. Instead, the thermal diffusion coefficients are calculated during runtime, offering a more computationally efficient solution. A new subroutine was developed in Chemkin [14] to calculate the thermal diffusion coefficient. Results obtained using this approach are referred to as MA-MA.

2.5 NGA

NGA solves Eqs. $2.1 - 2.5$, which represent the low Mach number reactive flow approximation. This solver can handle one-dimensional (1D), two-dimensional (2D), and three-dimensional (3D) flows, and it supports Cartesian, cylindrical, and spherical coordinate systems. Before discussing the solver, it is important to understand how the variables are defined and stored within it. In projection methods, staggered finite difference grids are commonly used.

In a staggered grid setup, each velocity component is defined on its own grid, while scalars, including pressure, are defined on a separate grid. Additionally, time staggering is implemented, meaning that the velocity vector and scalar fields are updated at different time intervals. Consider a 1D configuration with homogenous grid spacing h and constant time step Δt, as shown in

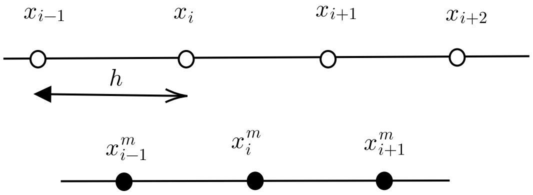

Figure 2.1: Representation of staggering in space.

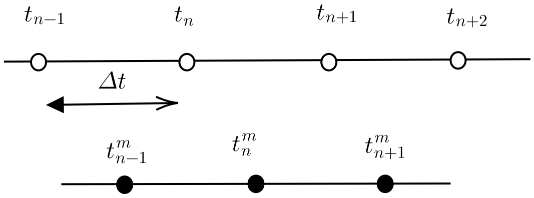

Figure 2.2: Representation of staggering in time.

Figs. 2.1 and 2.2.

Time is indexed by n on two distinct time sequences: one for velocity components and one for scalars. component u^n is an approximation at t^n, while ρ^n and Y^n are approximations at $t^m_n = \frac{t_n+t_{n+1}}{2}$. Below a description of time integration is presented.

2.5.1 Time step description

NGA uses a second-order in time semi-implicit Crank-Nicolson scheme to advance Eqs. 2.1-2.5 in time. The methodology used for advancing in time is given in Fig. 2.3. For this, assume a time step of Δt. Let us suppose that we have the solution at the previous time step, which will be used to solve for the solution at the new time step. This solver uses a sub-iteration mechanism to converge the solution, i.e., $k = [1, 2, 3, ..., Q]$, where Q is predefined. In this

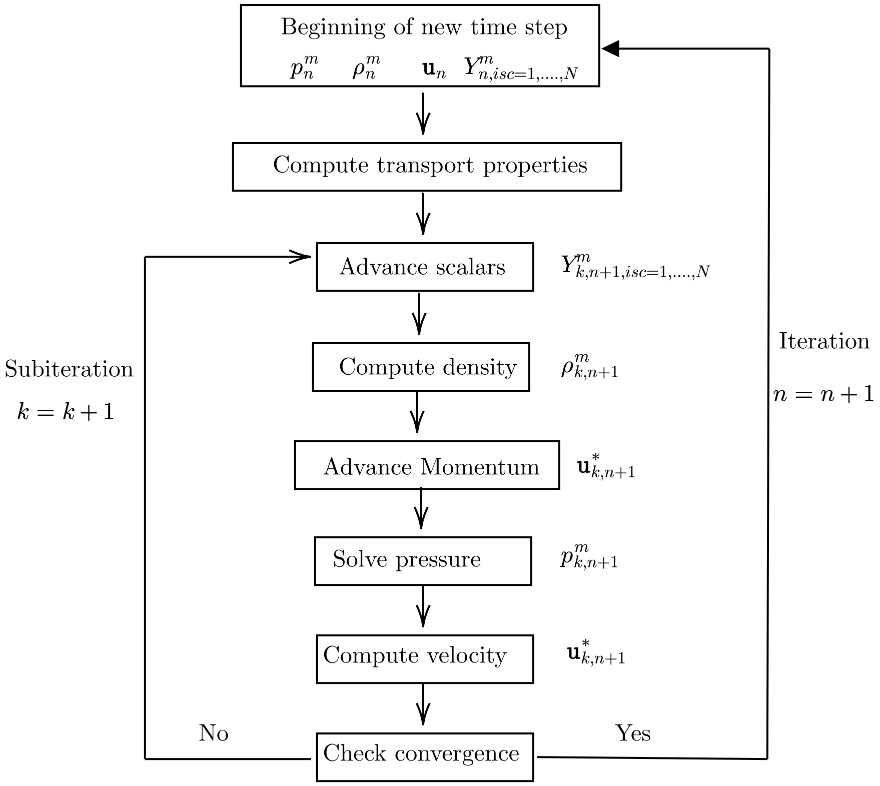

Figure 2.3: Flow chart representation of time advancement of NGA solver.

work, all the results presented use $Q = 3$. For each sub-iteration, the six steps are solved, as shown in Fig. 2.3. All these steps are explained in detail by Schlup [28].

2.6 NGA initialization

In all simulations, cylindrical expanding flames are used, with the chamber radius set to $R_w = 1\,\mathrm{m}$ (i.e., the computational domain is $0 \leq r \leq 1\,\mathrm{m}$).

As a result, the pressure increase (less than 0.01%) and compression-induced flow [32] are negligible. The flame is simulated only in the radial direction, assuming uniformity across the cylindrical expanding flame. This assumption allows for solving the setup in the radial direction alone, reducing the simulation to a one-dimensional (1D) domain rather than a full three-dimensional (3D) domain, as the three-dimensional (3D) domain would require significantly more computational resources.

To simulate in the radial direction, the solution from Cantera [7] is mapped onto the cylindrical flame at an initial radius r_0. This initial solution is then evolved over time until the required simulation time is reached. A detailed explanation of the initialization radius is provided in Section 3.4.1. This approach is preferred over direct flame ignition due to the irregularities observed in flame profiles at different minimum ignition energies (MIE) [24].

Previous simulations have shown that the domain size must be significantly larger than the flame thickness. Homogeneous discretization of a large domain is not an ideal choice, as it increases the number of grid points and, consequently, the computational cost. Therefore, non-uniform discretization is employed, using a hyperbolic tangent function to determine the grid size at each point. The actual grid profile is shifted to position the transition region away from the area of interest.

It is crucial to ensure that the region of interest does not coincide with the transition zone, as variations in grid size can cause interpolation instabilities. Through preliminary analysis, the maximum flame propagation

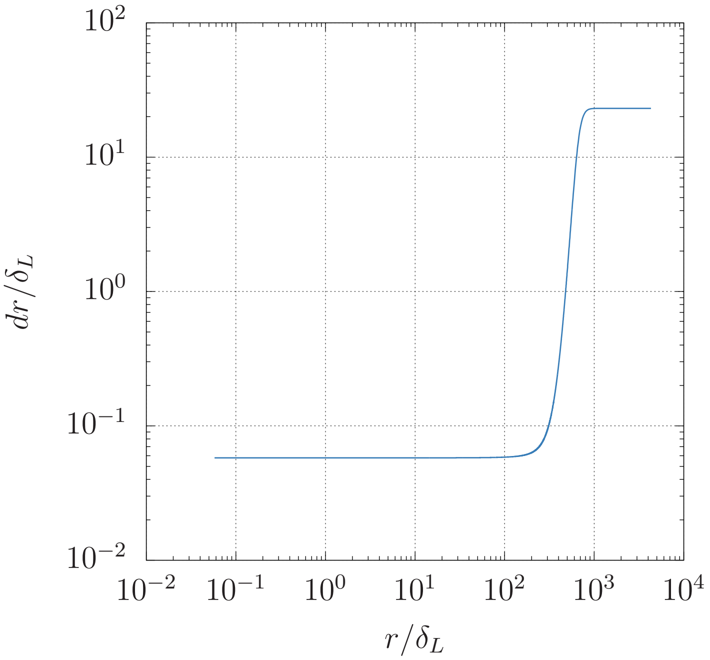

Figure 2.4: Grid spacing Δr along length normalized by flame thickness r/δ_L.

distance was calculated, ensuring that the transition in grid spacing occurs beyond the region of interest. Fig. 2.4 illustrates the grid spacing along the computational domain. It can be clearly observed that the transition in grid spacing occurs after approximately 200 flame thicknesses.

2.7 NGA post-processing

Running the simulation provides only the raw data (i.e., ρ, V, T, Y). Post-processing this raw data to obtain results takes considerable time to understand. As disccussed in Section 2.5, scalars are stored at time t_n^m and centered location (x^m), while velocities are stored at time t_n and staggered location (x), where $t_n^m = t_n + \Delta t/2$.

The following demonstration explains how the quantities are calculated for the flame displacement speed (FDS) relations discussed in Section 1.8. The flame surface is defined using temperature. A set of temperatures are chosen, and from this point onward, the temperature T^* is normalized by the unburnt temperature T_u, resulting in T^* ranging from 1 to the maximum temperature ratio within the flame. For a given T^* at time t_1, the position r_1 is calculated using interpolation. Similarly, for same T^* at time t_2, the position r_2 is determined. This process is also repeated for calculating densities. The radial location of flame for targeted T^* at time $t = t_n$ is evaluated as

$$r_n = \frac{r_n^m(T^*) + r_{n-1}^m(T^*)}{2}, \tag{2.18}$$

is a second-order accurate approximation, where r_n^m and r_{n-1}^m is radial location of flame for targeted T^*, calculated using the linear interpolation at time t_n^m and t_{n-1}^m. The dr/dt is approximated using second order accurate central differencing as

$$\left.\frac{dr}{dt}\right|_{t=t_n} = \frac{r_{n+1}(T^*) - r_{n-1}(T^*)}{\Delta t}. \tag{2.19}$$

From dr/dt the stretch rate at time t_n is calculated as

$$\mathbb{K} = \left.\frac{1}{r}\frac{dr}{dt}\right|_{t=t_n}. \tag{2.20}$$

An alternate way to write flame displacement speed, considering the flame as wave that propagates normal to itself against the fresh mixture, is evaluated at time t_n and centered location x^m as

$$S_d^u\bigg|_{t=t_n} = \frac{dr}{dt}\bigg|_{t=t_n} - v_r\bigg|_{t=t_n}, \tag{2.21}$$

It is normalized by ratio of local density (ρ) to density of fresh mixture (ρ_u) to obtain

$$\widetilde{S}_d^u = \frac{\rho S_d}{\rho_u}, \tag{2.22}$$

where the local density at time t_n is evaluated as

$$\rho_n\bigg|_{t=t_n} = \frac{\rho_n^m + \rho_{n-1}^m}{2}. \tag{2.23}$$

Finally, FDS is divided by laminar speed $\widetilde{S}_d/S_L$ to get dimensionless quantity, similarly for stretched rate it is nondimensionalized by multiplying the flame thickness and dividing by laminar flame speed $\delta_L\mathbb{K}/S_L$. The unstretched laminar flame speed (S_L) and flame thickness (δ_L) is calculated from 1D NGA run simulation. The quantities expressed above i.e. $\widetilde{S}_d/S_L$ and $\delta_L\mathbb{K}/S_L$ are plotted, the slope of this fitted lines is $\mathcal{L}/\delta_L$, as explained in Section 1.8. Finally, the Markstein number $\mathcal{M} = \mathcal{L}/l_f$, is obtained by multiplying the slope of Eq. 1.16 with δ_L/l_f, which is expressed as

$$\mathcal{M} = \frac{\mathcal{L}}{\delta_L}\frac{\delta_L}{l_f} = \frac{\mathcal{L}}{l_f}. \tag{2.24}$$

The Markstein number denotes the sensitivity of a flame to stretch, The value of the Markstein number is of the order of unity. The similar methodology is used when the Markstein number is calculated using FS relation.

Chapter 3

Validation

This chapter details the validation process of the solver for both hydrogen/air and propane/air premixed mixtures, ensuring accuracy in representing reactive flow dynamics. It includes a convergence study focused on numerical stability and accuracy. Additionally, the chapter explores the influence of flame initiation on flame speed specifically for the premixed hydrogen/air mixture.

3.1 Convergence Study

This chapter details the validation process of the solver for both hydrogen/air and propane/air premixed mixtures, ensuring accuracy in representing reactive flow dynamics. It includes a convergence study focused on numerical stability and accuracy. Additionally, the chapter explores the influence of flame initiation on flame speed, specifically for the premixed hydrogen/air mixture.

3.2 Convergence Study

A convergence study is a crucial part of numerical analysis and simulations, ensuring that the results of a computational model are reliable as the mesh is refined or as the time step size is decreased. It validates that the solution approaches a stable value, which is indicative of the model's accuracy.

Firstly, let's discuss the selection of mesh size (Δx). Our objective is to study the flame structure and flame propagation for different iso-surfaces in the flame. Therefore, the mesh size should be smaller than the flame thickness (δ_L) (shown in Table 3.1), since we need to use interpolation for finding the radius of the flame (r) for a particular iso-surface at a given time. It has been observed that there should be at least 15 points per flame.

Following the selection of an appropriate mesh size, it is equally important to determine an optimal time step (Δt) for our simulations. The time step needs to be small enough to accurately capture the dynamics of flame propagation and ensure numerical stability, yet large enough to make the computations feasible. For the study of flame structure and propagation, the time step size should be smaller than the flame time itself, while also considering the CFL conditions. Therefore, a study has been made to determine at which Δt the solution converges. The study considers a single mixture, named D89E65, at $T = 300$ K and $p = 1$ atm from Table 1.1. The mixture was simulated starting with a step size of 2 μs, gradually decreasing to the lowest possible value (computationally efficient). Table 3.1 shows the comparison between the Cantera and 1D NGA simulation results at different time step sizes. The difference is very small, which is a good indication that the solver is behaving correctly.

Table 3.1: Comparison of planar flame properties calculated by NGA with results from Cantera FLM mixture D89E65 ($T = 300$ K, $p = 1.000$ atm) with using mechanism by Hong et al. [10].

Cantera			1D NGA					
S_L (m/s)	δ_L (mm)	τ_L (ms)	Δt (μs)	Δx (μm)	Pts/fl	S_L (m/s)	δ_L (mm)	τ_L (ms)
1.0970	0.9520	0.8675	2	40	21	1.0821	0.92474	0.8546
			1	40	21	1.0845	0.9234	0.8515
			0.5	40	21	1.0856	0.92412	0.8513
			0.25	40	21	1.0861	0.92530	0.8519
			0.125	40	21	1.0863	0.92534	0.8518
			0.0625	40	21	1.0865	0.92500	0.8514

The convergence is studied by plotting the S_a^b and $\mathbb{K}$ for iso-surface $T^* = 3.56$ (where the maximum heat release rate is observed) for different step size defined in Table 3.1. The definitions of these quantities are explained in Section 1.9. From Fig. 3.1, it can be concluded that as the time step size decreases, the data converge with each other, which can be observed at $\Delta t = 0.125$ μs.

3.3 Premixed propane/air mixtures

Data from Giannakopoulos et al. [6] is used to validate the NGA solver, for a premixed propane/air mixture. The operating conditions and different mechanisms for which the results are available are shown below in Table 3.2. From Table 3.2, the results from the detailed 69-species mechanism are used

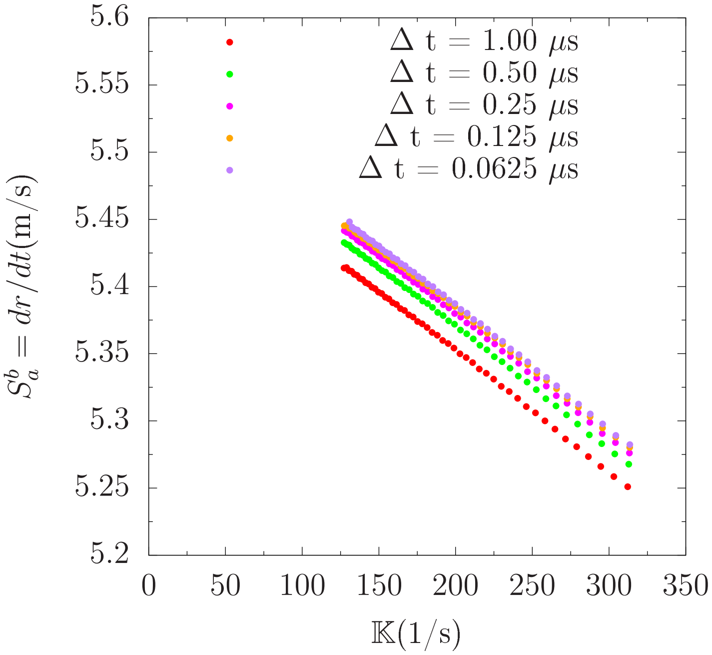

Figure 3.1: FDS S_a^b as a function of stretch rate $\mathbb{K}$ for $T^* = 3.56$ (max HRR) at different time step size for D89E65 mixture.

for validation. Since the Qin et al. [27] mechanism is no longer available, a mechanism with a similar number of species should be used for validation. Among the available mechanisms, the UCSD (University of California, San Diego) mechanism by Forman Williams [30] is chosen, as it contains 59 species, which is closer to the 69 species in the Qin et al. mechanism. Therefore, for this validation, the UCSD mechanism is used because it provides a more suitable comparison.

Firstly, it is necessary to verify the premixed unstretched (planar) flame properties calculated by NGA with results from Cantera [7]. In both NGA and Cantera the UCSD mechanism is used. In the NGA solver, the time step

Table 3.2: Mixture condition and chemical mechanisms for propane/air.

Mechanism	Species	T (K)	p (atm)	ϕ
Sun et al. - 1 step	5	298	1	1.0
Kim et al. - 1 step	5	298	1	1.0
Qin et al. Detailed	69	298	1	1.0

size is chosen to be 0.125 μs, as it has been shown in Section 3.2 that the solver converges at this time step. Here, a grid size of 20 μs is used, which corresponds to 20 points per flame. Table 3.3 presents the comparison of premixed unstretched flame properties calculated by NGA and results from Cantera [7]. The flame speed in NGA is calculated by plotting the distance traveled by the flame versus time, fitting a line through all the points, and determining the slope of the line. This is shown in Fig. 3.2 for the configuration presented in Table 3.3.

Table 3.3: Comparison of planar flame properties calculated by NGA with results from Cantera for propane/air mixture (T = 298 K, p = 1.000 atm, ϕ = 1) with using UCSD mechanism.

Cantera			1D NGA					
S_L (m/s)	δ_L (mm)	τ_L (ms)	dt (μs)	dx (μm)	Pts/Fl	S_L (m/s)	δ_L (mm)	τ_L (ms)
0.416	0.3685	0.8860	0.125	20	17	0.4405	0.3409	0.7739

The simulation was performed for cylindrical outward propagating flames of a propane/air mixture with a stoichiometric equivalence ratio, under oper-

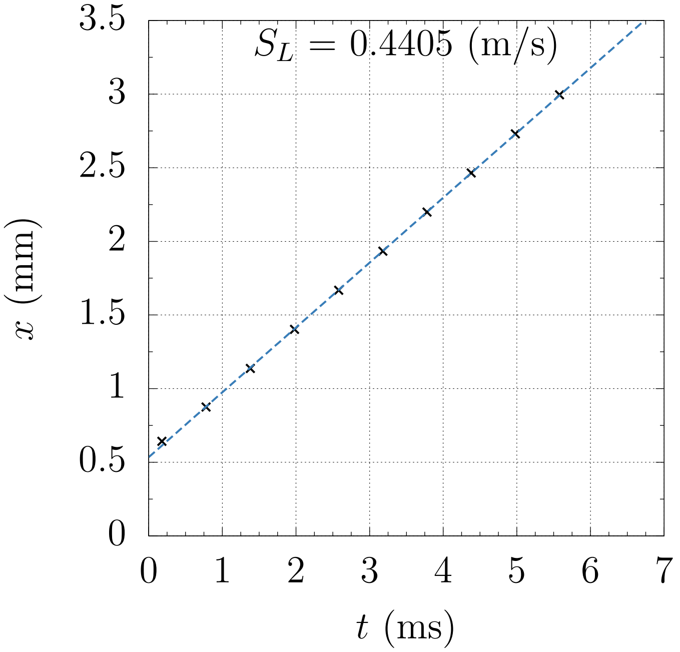

Figure 3.2: Distance traveled by flame as a function of time for propane/air mixture ($T = 298$ K, $p = 1.000$ atm, $\phi = 1$).

ating conditions of $p = 1$ atm and $T = 298$ K.

The cylindrical outward propagating flame was initialized using the parameters from Table 3.3, with a time step size of 0.125 μs and a starting grid spacing of 20 μm, with a domain length of 1.0 m. The flame was simulated until 10 ms to match the data from Giannakopoulos et al. [6]. By using variable grid spacing, the number of points was reduced from 50,000 to 5,837.

The temperature ratio (T^*) profiles along the normalized length (r/δ_L) for normalized time (t/τ_L) at intervals of 0.75, starting from 3.93 to the end of the simulation at 17.60 (equivalent to 15 ms), are shown in red lines, along with the profiles from Giannakopoulos et al. [6] shown in blue lines in Fig. 3.3. Some discrepancies are observed in the burnt gas temperature compared to the profiles from Giannakopoulos et al. [6].

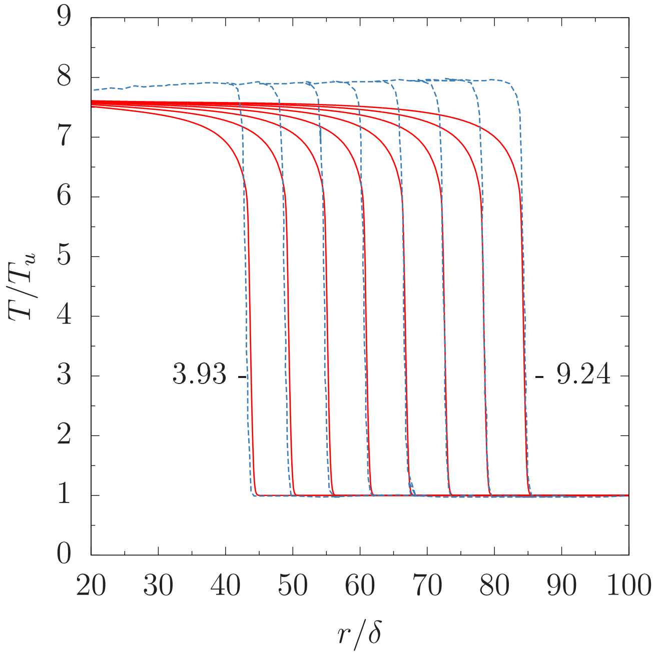

Figure 3.3: Temperature ratio profiles at time intervals of 0.75 (t/τ_L), red solid line represents the profiles using UCSD mechanism across a cylindrical-expanding flame and blue dashed line represents profiles from Giannakopoulos et al. [6] across a spherically-expanding flame.

To study how the Markstein number changes for different iso-surfaces, chosen as

$$T^* = [1.01, 1.10, 1.30, 1.50, 2.00, 4.00, 6.00], \tag{3.1}$$

the FDS relation, as discussed in Section 1.8, is used for calculation of properties. Fig. 3.4 shows the normalized FDS $(\widetilde{S}_d/S_L)$ along with the dimen-

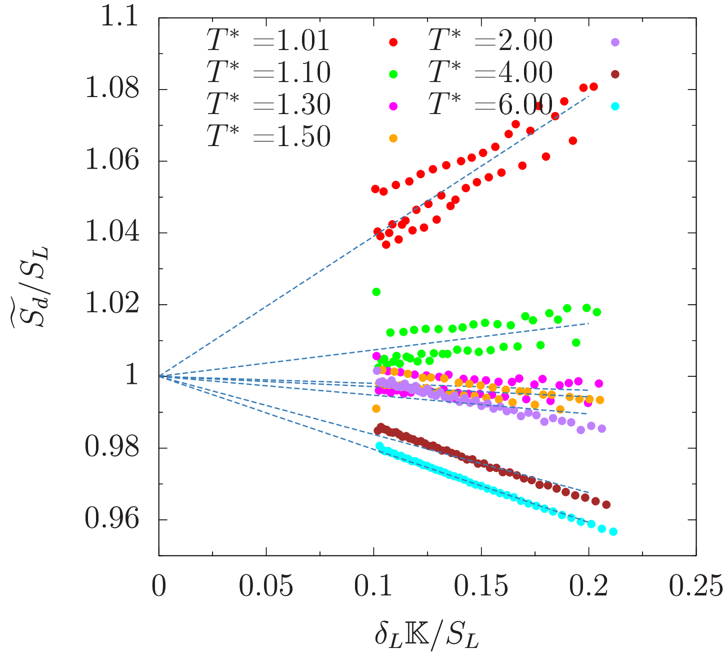

Figure 3.4: Normalized FDS ($\widetilde{S}_d/S_L$) as a function of dimensionless stretch rate ($\delta_L\mathbb{K}/S_L$) for different progress variables using the UCSD mechanism. Regression lines are drawn to the scattered data.

sionless stretch rate ($\delta\mathbb{K}/S_L$) for different progress variables. The slope of the regression lines, $\mathcal{L}/\delta_L$, when multiplied by δ_L, gives the Markstein lengths $\mathcal{L}$. In the preheat zone of the flame front, characterized by temperatures ($1.01 < T^* \leq 4$), the Markstein length exhibits variability in response to slight variations in the temperatures. However, within the reaction zone ($4 \leq T^* \leq 6$), the Markstein length converges to the same value. The scattering of data in Fig. 3.4 is due to error introduced by numerical interpolation to determine the values of S_d^u and $\mathbb{K}$.

The maximum heat release rate (HRR) for the progress variable $T^* =$

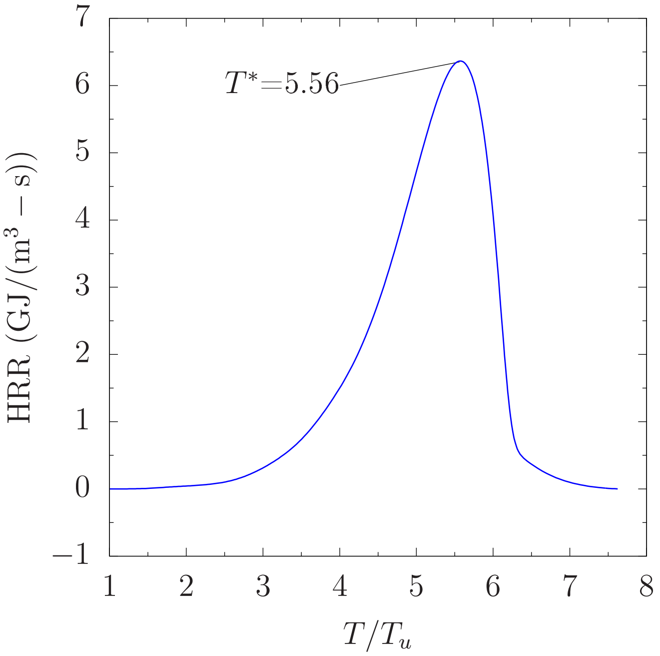

Figure 3.5: Heat release rate (HRR) from the 1D Cantera solution along the temperature ratio (T/T_u) for the UCSD mechanism.

5.56 was found by plotting HRR against the temperature ratio, as shown in Fig. 3.5.

To find the Markstein number, the slopes of the regression lines $\mathcal{L}/\delta_L$ are multiplied by δ_L/l_f as discussed in Eq. 1.16, where l_f is the flame thickness defined by the diffusion length, i.e., $l_f = D^u_{th}/S_L$, where D^u_{th} is the thermal diffusivity of the unburnt gas. The Markstein numbers calculated by NGA (using UCSD mechanism) has compared with the data from Giannakopoulos et al. (using Qin et al. [27] mechanism) [6] for different T^*, as shown in Fig. 3.6. Even though results from NGA yield slightly different Markstein numbers, the behavior of T^* near the unburnt or burnt sides of the flame remains consistent

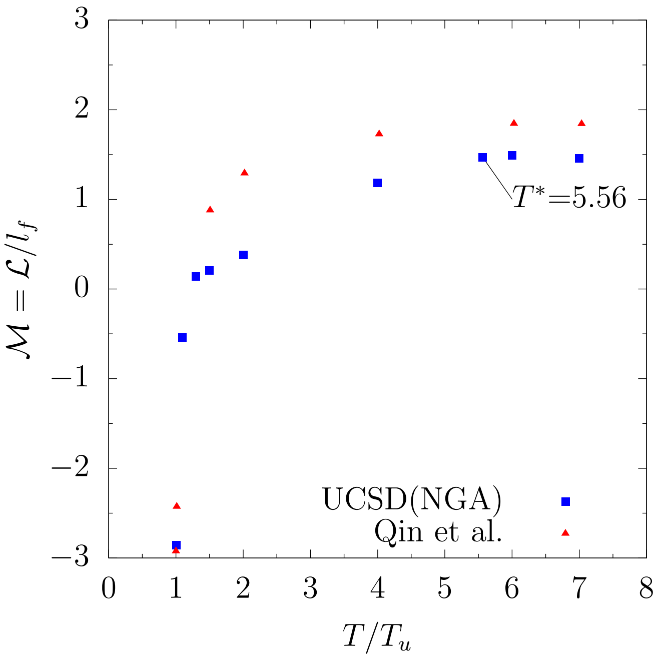

Figure 3.6: Markstein numbers comparison for Qin et al. (data from Giannakopoulos et al. [6]) [27] and UCSD (calculated by NGA) mechanisms along T^* for propane/air.

across the UCSD and Qin et al. [27] mechanisms. Additionally, Markstein numbers are sensitive to D_{th}^u; using different mechanisms might change the values of it.

3.4 Premixed hydrogen/air mixtures

In the study of flame/stretch interactions of premixed flames by Kwon et al. [20], some data is available for helium-diluted mixtures. However, there are significant uncertainties in calculating the Markstein numbers or Markstein lengths, as some constants are not properly defined. Apart from this study, there is no experimental or numerical data available in the literature for these mixtures, so there is no data to validate the results. Therefore, we are left with the task of validating the results with hydrogen/air mixtures, for which numerous studies are available. One such study is by Liang et al. [24], where they plotted the Markstein number for different ranges of lean and rich hydrogen/air mixtures, and compared them with experimental data. The experimental results presented by Liang et al. [24] are from Taylor [29] and Aung et al. [1]. Results from Liang et al. [24] were obtained using a solver named A-SURF, which solves the conservation equations for one-dimensional, compressible, multi-component, reactive flow in spherical coordinates using the finite volume method and the detailed chemistry of Li et al. [23]. They also addressed the effect of the Soret effect on the Markstein length.

Lean premixed hydrogen/air mixtures with different equivalence ratios (ϕ) at T = 298 K and P = 1 atm were studied by Liang et al. [24], but we are considering only $\phi = 0.5$, 0.6, 0.7, and 0.9. Flame properties calculated by NGA are compared with the results from Cantera [7] for different mixtures, as shown in Table 3.4. The mixtures are named as EXX, where XX is $\phi \times 100$. The NGA results are simulated with converged temporal resolution, i.e., $\Delta t = 0.125\ \mu s$, as discussed in the convergence study, and spatial resolution, i.e., $\Delta x = 20\ \mu m$, consistent with a minimum of 20 points per flame thickness. The same mechanism by Li et al. [23] is used in NGA. The flame properties using NGA are calculated as discussed before.

Table 3.4: Comparison of planar flame properties calculated by NGA with results from Cantera for H_2/air at different equivalence ratios, with mixture conditions of $T = 298$ K and $P = 1$ atm.

Mixture			Cantera			NGA		
Name	ϕ	σ	S_L (m/s)	δ_L (mm)	τ_L (ms)	S_L (m/s)	δ_L (mm)	τ_L (ms)
E50	0.50	4.879	0.511	0.4314	0.8446	0.5601	0.4180	0.7464
E60	0.60	5.425	0.887	0.3700	0.417	0.9222	0.3654	0.3963
E70	0.70	5.903	1.298	0.3514	0.2708	1.3136	0.3496	0.2166
E90	0.90	6.599	1.780	0.3463	0.1945	2.004	0.3529	0.1760

3.4.1 Flame initiation

For the validation of the premixed propane/air mixture results, the flame has to be initialized at $r/\delta_L = 15$. In this analysis, the aim is to verify whether the initialization of the flame at different radii affects the flame speed (S_a^b) in relation to the stretch rate ($\mathbb{K}$) as the stretch rate approaches zero. The flame is initialized at different radii: $r/\delta_L = 2, 5, 10, 15$, and 20. The mixture chosen here is E50, from Table 3.4. As shown in Fig. 3.7, even though the profiles differ for each radius at higher stretch rates, they all converge to a single profile as $\mathbb{K} \rightarrow 0$, i.e., at lower stretch rates. Since we are interested in studying the flame response to stretch at lower stretch rates, the flame initialization does not have any effect on the flame.

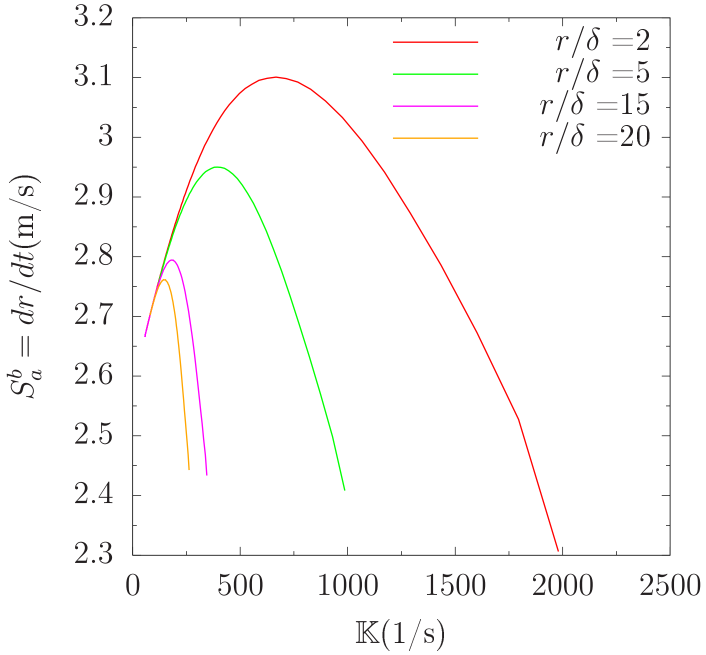

Figure 3.7: Comparison of flame speed as a function of stretch rate for different flame initialization radii r/δ_L.

3.4.2 Markstein lengths

Markstein theory is valid only at lower stretch rates; hence, the theory is applied in the lower stretch rate regime, where the profile remains linear. For the E50 case from Table 3.4, the normalized flame speed (S_a^b/S_L^b) is plotted against the dimensionless stretch rate ($\delta_L \mathbb{K}/S_L^b$) as shown in Fig. 3.8. The slope of the line represents the Markstein number ($\mathcal{M}^b$), which is then multiplied by the flame thickness δ_L to obtain the Markstein length ($\mathcal{L}^b$).

Fig. 3.9 compares the Markstein numbers calculated by NGA with A-SURF [24] and experiments for $\phi = 0.5$, 0.6, 0.7, and 0.9. There is good agree-

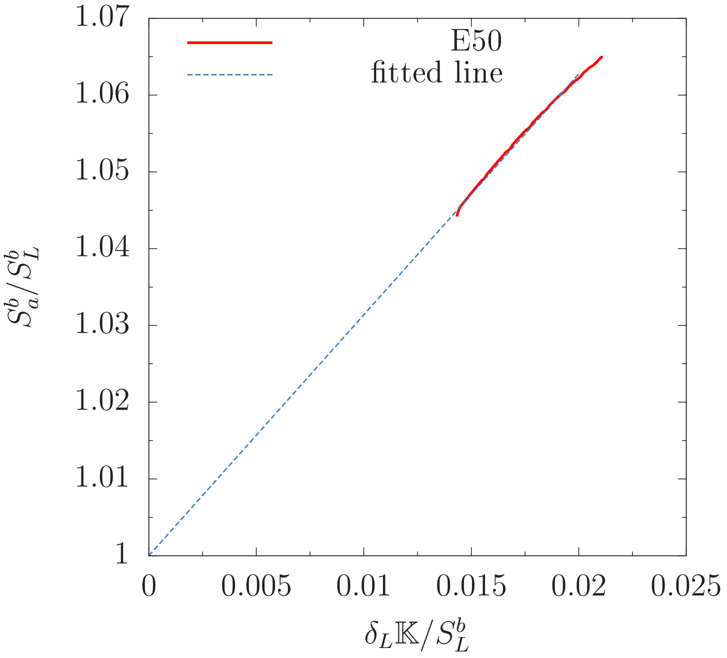

Figure 3.8: Normalized flame speed (S_a^b/S_L^b) as a function of dimensionless stretch rate ($\delta_L \mathbb{K}/S_L^b$) for E50 at $T = 298$ K and $P = 1$ atm.

ment between the results, with minor differences attributed to the fact that A-SURF uses a multicomponent transport model, while in NGA a mixture-averaged model is used.

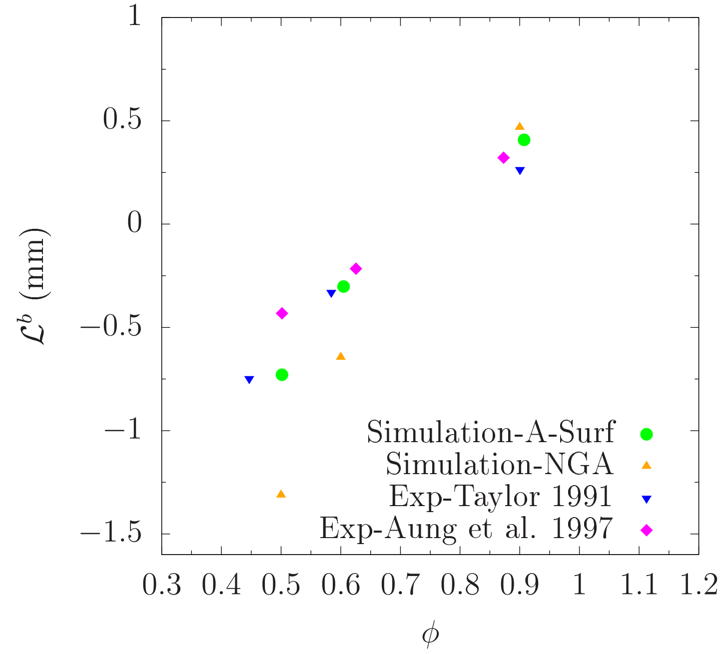

Figure 3.9: Comparison of Markstein numbers ($\mathcal{L}^b$) calculated by NGA with available experimental and simulation data for different equivalence ratios (ϕ).

Chapter 4

Results and conclusions

This chapter presents the final analysis of the flame properties for the selected mixtures, which are discussed in in Section 1.11. Additionally, it highlights key conclusions derived from the findings of this work and the future work, offering a comprehensive summary of the research outcomes and their implications.

4.1 Results

As discussed in Chapter 3, the methodology and solver have been validated using existing literature results. After successful validation, the methodology is now applied to the selected mixtures. Before jumping directly to the final results, let us discuss the flame propagation for one of the mixtures from Table 1.1. Consider D89E65 with $p = 2$ atm. For all the results presented in this section, the flame was initialized at $r/\delta_L = 15$. Section 3.4.1 tells us that flame initiation does not affect the flame propagation at lower stretch rates. The temperature ratio T^* profiles along the normalized length (r/δ_L) for normalized time $(t/\tau_L$, number of flame times) from 1 to the end of the simulation (22, i.e., until 10 ms) are shown in Fig. 4.1.

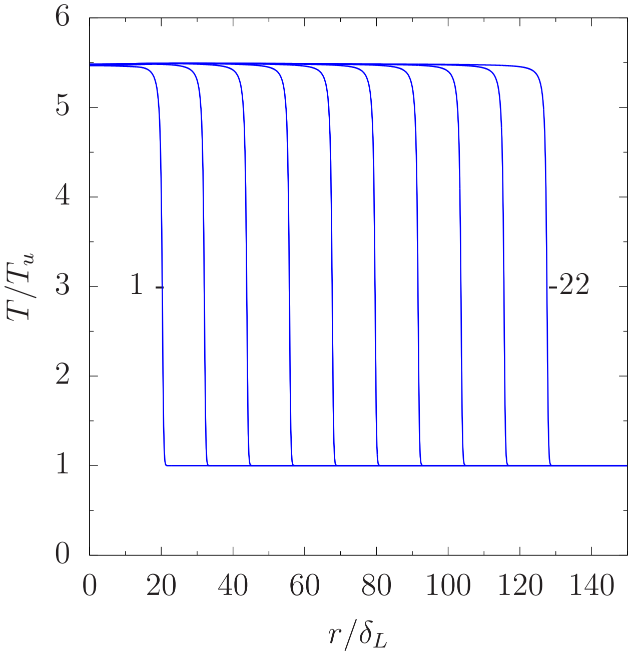

Figure 4.1: Temperature ratio profile along the domain starting from time $t/\tau_L = 1$ to $t/\tau_L = 22$ for D89E65 at $p = 2$ atm.

The flame is located based on the temperature at maximum heat release rate (HRR). These T^* values are reported in Table 4.1 for each mixture. For the D89E65 mixture at $p = 2$ atm, the flame speed S_a^b as a function of the stretch rate $\mathbb{K}$ is presented in Fig. 4.2. It can be observed that at higher stretch rates (i.e., where the flame is initiated), some irregularities appear in the profile. However, after a certain point, the profile stabilizes and transitions to a linear trend.

As discussed in Section 2.3, the Soret effect plays a role where there is heavy or light fuel in the mixtures, briefly discussed by Liang et al. [24]. There is a need to compare the results with and without the Soret effect.

Table 4.1: Tabulated values for T^* at maximum HRR for the selected mixtures.

Name	p_0 (atm)	T/T_u max HRR
D80E95	1	4.2398
D82E90	1	4.1720
D84E90	1	4.0838
D89E65	1	3.5600
	2	3.9114
	3	4.0262

Two models of the Soret effect are implemented in the NGA solver: one is MA-MC for the multicomponent model Soret effect, and the other is MA-MA for the mixture average Soret effect as discussed in Section 2.3. We are interested in finding the Markstein number ($\mathcal{M}^b$) based on the burnt side; the relation is given in Eq. 1.20. The Markstein number is calculated by plotting the normalized flame speed (S_a^b/S_L^b) along the dimensionless stretch rate ($\delta_L \mathbb{K}/S_L^b$), finding the slope of the regression line. Fig. 4.3 shows the flame response over stretch for three different methods: MA mixture average without the Soret effect, MA-MA mixture average Soret model, and MA-MC multicomponent Soret model. Since the normalized flame speed increases as stretch decreases (radius increases), from Markstein theory, this mixture has a positive Markstein number ($\mathcal{M}^b > 1$). Fig. 4.3 also shows that there is an influence of including the Soret effect.

It is also necessary to study the flame response to stretch for the flame displacement speed relation in Section 2.21. Normalized FDS ($\widetilde{S_d}/S_L$) along di-

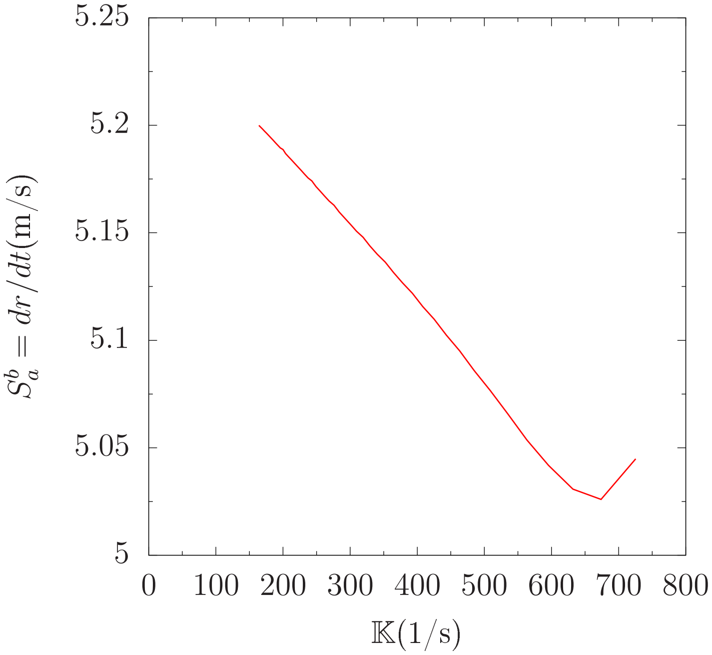

Figure 4.2: Flame speed S_a^b as a function of stretch rate $\mathbb{K}$ for D89E65 at $p = 2$ atm.

mensionless stretch rate ($\delta_L \mathbb{K}/S_L$) for different iso-surfaces is shown in Fig. 4.4 for D89E65 at 2 atm. In the preheat zone of the flame front, characterized by temperatures ($1.01 < T^* \leq 2$), the Markstein length exhibits variability in response to slight variations in the temperatures. However, within the reaction zone ($2 \leq T^* \leq 5$), the Markstein length converges to the same value, $T^* = 3.9$, where maximum HRR is observed. This also gives the first iso-surface, leading to the unburnt mixture getting slower, which results in a thinner flame as time progresses.

The flame response is consistent across all mixtures; however, each mixture differs in laminar flame speed (S_L) and Markstein number ($\mathcal{M}^b$), as

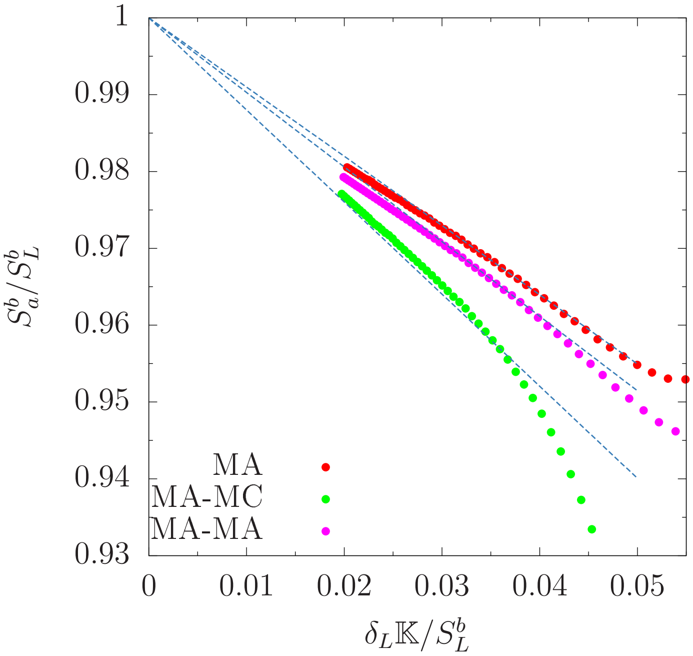

Figure 4.3: Normalized flame speed (S_a^b/S_L^b) as a function of dimensionless stretch rate ($\delta_L \mathbb{K}/S_L^b$) for D89E65 at $p = 2$ atm.

reported in Table 4.2. From these results, it is evident that the inclusion of the Soret effect significantly influences the flame properties. Specifically, there is a substantial difference in the Markstein numbers when the Soret effect is included, while the impact on laminar flame speed is relatively minor. Notably, the Markstein numbers are higher in the MA-MC method compared to the MA-MA method. The MA-MC method involves coupling the multicomponent Soret model with mixture-average transport, which may introduce some inconsistencies, potentially indicating issues with the model. Furthermore, the MA-MC method is computationally more expensive to solve than the MA-MA method.

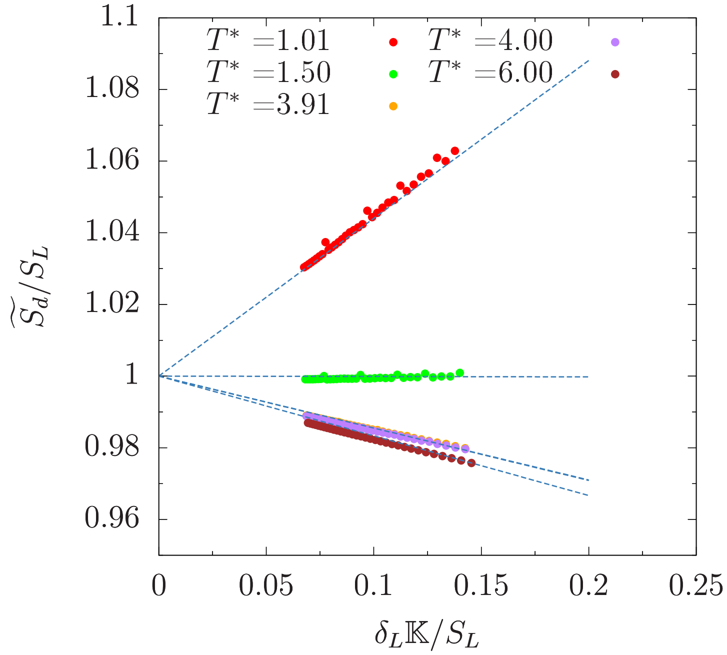

Figure 4.4: Normalized FDS ($\widetilde{S_d}/S_L$) as a function of dimensionless stretch rate ($\delta_L\mathbb{K}/S_L$) using FDS relation for D89E65 at $p = 2$ atm.

One observable trend is that mixtures with higher laminar flame speeds tend to have higher Markstein numbers ($\mathcal{M}^b$). This behavior can be understood by considering that the Markstein number is a measure of the sensitivity of flame propagation to stretch effects, such as curvature and strain. A higher Markstein number indicates a flame that is more resistant to stretch, leading to greater stability. Therefore, mixtures with higher flame speeds, which generally correspond to conditions with optimal reactivity and faster consumption of fuel, are also characterized by a greater ability to resist perturbations due to their larger Markstein numbers.

Additionally, as the equivalence ratio (ϕ) increases from lean mixtures with $\phi = 0.65$ towards stoichiometric conditions with $\phi = 0.95$, the laminar flame speed also increases. This can be attributed to the fact that at higher equivalence ratios, there is more fuel available in the mixture, which enhances the rate of chemical reactions. An increased reaction rate leads to a higher release of thermal energy, which accelerates the propagation of the flame front.

However, when the mixture becomes too rich (beyond stoichiometry), the flame speed may eventually decrease due to reduced oxygen availability, which limits combustion efficiency. The above discussion may change for other fuels.

Table 4.2: Laminar flame speeds and Markstein numbers for various mixtures calculated by different models for FLM mixtures at $T_u = 300$ K.

Mixture		MA		MA-MC		MA-MA	
Name	p_0 (atm)	S_L (m/s)	$\mathcal{M}^b$	S_L (m/s)	$\mathcal{M}^b$	S_L (m/s)	$\mathcal{M}^b$
D80E95	1	3.6894	2.7282	3.772	4.4887	3.6990	3.0011
D82E90	1	3.2013	2.6941	3.2797	4.2494	3.2156	2.9735
D84E90	1	2.8169	2.6861	2.8856	4.2689	2.8318	3.0155
D89E65	1	1.0863	0.9635	1.0986	1.2127	1.0986	1.2127
	2	1.0273	0.9010	1.0427	1.1986	1.0381	0.9708
	3	0.9626	0.8340	0.9744	1.1514	0.9714	0.9051

This research is a collaborative effort, with experiments on these mixtures conducted at the Gas Dynamics Imaging Laboratory at the University of Michigan, Ann Arbor [21]. The experimental setup uses spherical expanding flames. When comparing the numerical results with the experimental data, a 50% difference was observed. Additionally, for lower Markstein number cases, the experimental results showed negative Markstein numbers. However, the flame speeds calculated numerically were in agreement with the experimental results.

As discussed in the validation section, the numerical methodology used in this study has been validated against existing results for premixed propane/air and hydrogen/air mixtures. Despite the validation, modeling the experimental setup remains challenging due to several uncertainties. The spherical expanding flame configuration is sensitive to small variations in initial conditions, such as mixture homogeneity and ignition timing, which can introduce discrepancies. Furthermore, factors like temperature gradients, pressure variations, and convective effects can affect the flame's behavior. The difficulty in accurately measuring flame stretch and instability, especially at lower Markstein numbers, can also lead to negative values. Experimental measurement errors, instrument calibration issues, and noise add to the uncertainty, making it difficult to match theoretical predictions precisely. Despite these challenges, the laminar flame speed measurements remained consistent, suggesting that the fundamental combustion dynamics were captured accurately.

4.2 Conclusion

This report investigates the Markstein number and laminar flame speed by validating results from the existing literature using various flame models.

A framework for 1D flame propagation, based on "Premixed" (Cantera [7]), is mapped onto cylindrical propagating flames, avoiding solver instabilities typically encountered during ignition. To simulate constant pressure flames, a large computational domain with a variable mesh is employed, refining the mesh in regions of interest.

The mixture-average (MA) model within NGA was validated for both premixed propane-air and hydrogen/air mixtures. A significant challenge in this work was validating the mixture-average model against the studies of Giannakopoulos et al. [6] and Liang et al. [24]. The Soret effect was also considered, particularly in mixtures with light or heavy fuels. Two models, the multi-component (MA-MC) and mixture-average (MA-MA), were implemented in NGA to include this effect. It was found that incorporating the Soret effect influenced the Markstein number, with the MA-MC model slightly over-predicting the values.

The study concludes that all the selected mixtures with unity Lewis numbers exhibit positive Markstein numbers. Notably, the mixture D89E65 ($\vartheta = 0.89$, $\phi = 0.65$) at various pressures showed a Markstein number close to 1. As the equivalence ratio (ϕ) increases from 0.65 to 0.95, the laminar flame speed increases, which in turn raises the Markstein number. Finally, comparing the simulated results with experimental data revealed significant discrepancies in the Markstein numbers. However, the laminar flame speed remained relatively consistent, suggesting that while the Markstein numbers are sensitive to model assumptions and input parameters.

4.3 Future Work

The framework developed in this work for simulating constant pressure cylindrical propagating flames, by utilizing a large domain with a variable mesh, has encountered several numerical challenges. Specifically, the numerical schemes occasionally result in solver crashes, which can occur in both the pressure solver and the combustion model. These issues point to the need for a dedicated study to further investigate the underlying causes of these instabilities.

Moreover, the influence of thermal diffusion on the Markstein number has been observed, particularly in how the flame speed responds to stretch. While the designed mixture-average (MA-MA) and multi-component (MA-MC) models provide valuable insights, they have yet to be validated against existing experimental data. Additionally, these models need further optimization to reduce computational costs compared to the traditional mixture-average (MA) model. Therefore, future work should focus on validating these models and improving their efficiency.

Appendices

Bibliography

[1] K.T. Aung, M.I. Hassan, and G.M. Faeth. Flame stretch interactions of laminar premixed hydrogen/air flames at normal temperature and pressure. *Combustion and Flame*, 109(1):1–24, 1997.

[2] Michael P. Burke, Marcos Chaos, Yiguang Ju, Frederick L. Dryer, and Stephen J. Klippenstein. Comprehensive h2/o2 kinetic model for high-pressure combustion. *International Journal of Chemical Kinetics*, 44(7):444–474, 2012.

[3] Sebastien M Candel and Thierry J Poinsot. Flame stretch and the balance equation for the flame area. *Combustion Science and Technology*, 70(1-3):1–15, 1990.

[4] Sydeny Chapman and T. G. Cowling. *The mathematical theory of non-uniform gases. an account of the kinetic theory of viscosity, thermal conduction and diffusion in gases.* 1970.

[5] Olivier Desjardins, Guillaume Blanquart, Guillaume Balarac, and Heinz Pitsch. High order conservative finite difference scheme for variable density low mach number turbulent flows. *Journal of Computational Physics*, 227(15):7125–7159, 2008.

[6] George K Giannakopoulos, Antonis Gatzoulis, Christos E Frouzakis, Moshe Matalon, and Ananias G Tomboulides. Consistent definitions of “flame displacement speed” and “markstein length” for premixed flame propagation. *Combustion and Flame*, 162(4):1249–1264, 2015.

[7] David G. Goodwin, Harry K. Moffat, Ingmar Schoegl, Raymond L. Speth, and Bryan W. Weber. Cantera: An object-oriented software toolkit for chemical kinetics, thermodynamics, and transport processes. `https://www.cantera.org`, 2023. Version 3.0.0.

[8] J. Hirschfelder, C. F. Curtiss, and R. B. Bird. *Molecular Theory of Gases and Liquids*. John Wiley & Sons, New York, 1954.

[9] J. O. Hirschfelder, Charles F. . Curtiss, and R. Byron Bird. Molecular theory of gases and liquids. 1954.

[10] Zekai Hong, David F. Davidson, and Ronald K. Hanson. An improved h2/o2 mechanism based on recent shock tube/laser absorption measurements. *Combustion and Flame*, 158(4):633–644, 2011. Special Issue on Kinetics.

[11] Jialong Huo, Sheng Yang, Zhuyin Ren, Delin Zhu, and Chung K. Law. Uncertainty reduction in laminar flame speed extrapolation for expanding spherical flames. *Combustion and Flame*, 189:155–162, 2018.

[12] International Energy Agency. Global Hydrogen Review 2023: Executive Summary, October 2023. Accessed: 2024-10-31.

[13] R. J. Kee, M. E. Coltrin, and P. Glarborg. *Chemically Reacting Flow: Theory and Practice*. Wiley-Interscience, Hoboken, NJ, USA, 2003.

[14] R. J. Kee, F. M. Rupley, and J. A. Miller. Chemkin-ii: A fortran chemical kinetics package for the analysis of gas-phase chemical kinetics. Technical Report SAND89-8009, Sandia National Laboratories, Livermore, California, 1989.

[15] Robert Kee, Graham Dixon-lewis, Jurgen Warnatz, Michael Coltrin, and James Miller. A fortran computer code package for the evaluation of gas-phase, multicomponent transport properties. 08 1996.

[16] Tejas Kulkarni and Fabrizio Bisetti. Analysis of the development of the flame brush in turbulent premixed spherical flames. *Combustion and Flame*, 234:111640, 2021.

[17] Tejas Kulkarni and Fabrizio Bisetti. Surface morphology and inner fractal cutoff scale of spherical turbulent premixed flames in decaying isotropic turbulence. *Proceedings of the Combustion Institute*, 38(2):2861–2868, 2021.

[18] Tejas Kulkarni, Romain Buttay, M. Houssem Kasbaoui, Antonio Attili, and Fabrizio Bisetti. Reynolds number scaling of burning rates in spherical turbulent premixed flames. *Journal of Fluid Mechanics*, 906:A2, 2021.

[19] Kenneth K. Kuo. *Principles of Combustion*. John Wiley & Sons, Hoboken, NJ, 2nd edition, 2005.

[20] O.C Kwon and G.M Faeth. Flame/stretch interactions of premixed hydrogen-fueled flames: measurements and predictions. *Combustion and Flame*, 124(4):590–610, 2001.

[21] Gas Dynamics Imaging Laboratory. Gas dynamics imaging laboratory - research, 2024. Accessed: December 2, 2024.

[22] Chung K. Law. *Combustion Physics*. Cambridge University Press, Cambridge, UK, 2006.

[23] Juan Li, Zhenwei Zhao, Andrei Kazakov, and Frederick L. Dryer. An updated comprehensive kinetic model of hydrogen combustion. *International Journal of Chemical Kinetics*, 36(10):566–575, 2004.

[24] Wenkai Liang, Chung K. Law, and Zheng Chen. Ignition of hydrogen/air mixtures by a heated kernel: Role of soret diffusion. *Combustion and Flame*, 197:416–422, 2018.

[25] Youhei Morinishi, Oleg V. Vasilyev, and Takeshi Ogi. Fully conservative finite difference scheme in cylindrical coordinates for incompressible flow simulations. *Journal of Computational Physics*, 197(2):686–710, 2004.

[26] Thierry Poinsot and Denis Veynante. *Theoretical and numerical combustion*. RT Edwards, Inc., 2005.

[27] Zhiwei Qin, Vitali V. Lissianski, Huixing Yang, William C. Gardiner, Scott G. Davis, and Hai Wang. Combustion chemistry of propane: A case study of detailed reaction mechanism optimization. *Proceedings of the Combustion Institute*, 28(2):1663–1669, 2000.

[28] Jason Schlup and Guillaume Blanquart. Validation of a mixture-averaged thermal diffusion model for premixed lean hydrogen flames. *Combustion Theory and Modelling*, 22(2):264–290, 2018.

[29] S.C. Taylor. *Burning Velocity and the Influence of Flame Stretch*. Doctoral dissertation, University of Leeds, 1991.

[30] San Diego (UCSD) University of California. Chemical-kinetic mechanisms for combustion applications. `https://web.eng.ucsd.edu/mae/groups/combustion/mechanism.html`, 2024. Accessed: October 2, 2024.

[31] Aditya Vinod, Tejas Kulkarni, and Fabrizio Bisetti. Reynolds number scaling and self-similarity of the surface density function of reactive-diffusive interfaces in shear-driven turbulence up to reλ=140. *Proceedings of the Combustion Institute*, 40(1):105694, 2024.

[32] M. P. Burke Z. Chen and Y. Ju. Effects of compression and stretch on the determination of laminar flame speeds using propagating spherical flames. *Combustion Theory and Modelling*, 13(2):343–364, 2009.